Università degli studi di Padova

Dipartimento di Fisica e Astronomia "Galileo Galilei"

Laboratori Nazionali di Legnaro - INFN - LNL

Corso di Laurea Magistrale in Fisica

Tesi di Laurea Magistrale

Optical Manipulation of the Magnetization in Ferrimagnetic YIG Samples

Relatore:
PDott.ssa Caterina Braggio
Supervisore Esterno:
Dott. Antonello Ortolan

Laureanda: Maja Colautti
Matricola: 14022080

Contents

CHAPTER 1

Introduction

The ultra-fast optical manipulation of the magnetic order has become a topic of great interest in modern magnetism. The feasibility of controlling the magnetization with light paves the way to potential applications ranging from high density magnetic data storage [1], spintronics [2], to quantum information processing [3], [4]. The frontier of the ultra-fast control of the magnetization precession is represented by experimental studies that involve ultra-short laser pulses (fs), that is the time domain of opto-magnetism. In these experiments, the high-intensity optical pulse generates a transient DC field in the material which twists the magnetization, and a second probe pulse allows for studying the induced magnetic changes.

This thesis describes a novel method for the full-optical control of the magnetization precession in a ferrimagnet, based on the utilization of a mode-locked laser system with repetition rates in the $\approx$GigaHertz range. This tecnique allows for sustaining the magnetization precession in the steady-state regime, condition that has not been realized in previous opto-magnetic experiments. The magnetic system responds to the optical laser excitation with a radiation field which is used to systematically investigate the phenomenon. The analysis is conducted in Yittrium-Iron garnet (YIG) samples by means of ferromagnetic resonance (FMR) techniques. Measurement are conducted in two different configurations, i.e. with the samples in free field couple to a single loop antenna (free field measurements) and in a cavity-QED framework, which is realized by enclosing the magnetic sample in a microwave resonator. In both cases the magnetization precession is optically driven by tuning the repetition rate of the picosecond laser pulses to the Larmor frequency of the magnetic sample. This condition is achieved through a previous characterization of the system in the frequency domain by means of microwave network analysis. As compared to the free field scheme, detection of the radiated field in the cavity during the laser action allows to estimate the radiated field amplitude by measuring the power absorbed by the sample.

In the cavity we accomplish a strong coupling regime between the magnetostatic modes of the YIG sample and the cavity mode. This regime is the so-called hybridization that can be described with a simple classical model of a pair of coupled harmonic oscillators.

In order to avoid thermal effects, investigation of the photoinduced magnetization precession is conducted using 1550 nm-wavelength laser pulses, in the transparency window of the YIG samples. The phenomenon is explained as originating from the non-linear inverse Faraday effect (IFE) where by laser light can modify the magnetization of the material. In the model that has been developed it is possible to simplify the thoretical description of the photoinduced magnetization vector, and the model is tested by investigating the intensity dependence of the emitted microwave field amplitude.

Most importantly, the signal dependence from the incident light polarization gives relevant signatures of the IFE.

CHAPTER 2

Ultrafast control of the magnetization

This thesis describes a novel method for the full-optical control of the magnetization precession in a ferrimagnet, based on the utilization of a multi-GHz laser system. Such a scheme allows for sustaining the magnetization precession in the steady-state regime, condition that has not been realized in previous opto-magnetic experiments. The phenomenon arises from opto-magnetic non-linear effects, and we investigate it in Yittrium-Iron garnet (YIG) samples by means of ferromagnetic resonance (FMR) techniques. In order to better control the involved physical observables, measurements are also conducted in a cavity-QED framework, which is realized by enclosing the magnetic sample in a microwave resonator. In this condition FMR magnetostatic modes of the YIG sample couple to the cavity mode and we optically drive the hybridized system that can be described with a simple classical model of a pair of coupled harmonic oscillators.

2.1 Review of magnetization dynamics

The macroscopic quantity we are interested in is the magnetization $\mathbf{M}$ of a magnetic material. This vector is the classical manifestation of the microscopic magnetic properties of the unpaired electrons in the material. Electrons behave indeed like magnetic dipoles [5], each carrying an angular momentum of electron spin $\mathbf{S}$ and possessing a magnetic dipole moment $\boldsymbol{\mu}$, given by

$$\boldsymbol{\mu} = -\frac{g_e q_e}{2m_e}\mathbf{S} = -\gamma_e \mathbf{S} \tag{2.1}$$

where g_e , q_e , m_e and γ_e are respectively the spin g-factor, the modulus of the charge, the mass, and the gyromagnetic ratio of the electron. The vectorial sum over each of the quantum-mechanical momenta of spin in the material gives the classical magnetization vector, normalized over the total volume V of the material

$$\mathbf{M} = \frac{\mu}{V}\sum_{i=1}^{N}\hat{J}_i\,. \tag{2.2}$$

This allows for a classical discussion of the problem in terms of one macroscopic spin, as first introduced by Bloch [6].
The energy of a magnetic dipole $\boldsymbol{\mu}$ in a given applied field $\mathbf{H_0}$ is $E = -\boldsymbol{\mu}\cdot\mathbf{H_0}$, and defines the minimal energy equilibrium position for the magnetic moment parallel to the field direction. At equilibrium, the magnetic moments of the electrons are thus aligned opposite to the field direction, due to the

negative sign of the electronic charge. If the magnetic moment is tilted of an angle θ with $\mathbf{H_0}$ by a small external force, one of the consequences of having a magnetic moment $\boldsymbol{\mu}$ proportional to the intrinsic angular momentum $\mathbf{J}$, is that the electronic magnet will precede. The moment $\boldsymbol{\mu}$ will indeed undergo a torque $\boldsymbol{\tau}$ equal to

$$\boldsymbol{\tau} = \boldsymbol{\mu} \times \mathbf{H_0} \tag{2.3}$$

which will try to bring it back to the equilibrium direction, causing the angular momentum vector $\mathbf{J}$ to precede about a cone. The angular velocity can be expressed as $\boldsymbol{\omega_0} = \frac{d\phi}{dt}\mathbf{u}$, being $\mathbf{u}$ the unitary vector along the istantaneous rotation axis. Since the rate of change of the angular momentum is equal to the exerted torque $\frac{d\mathbf{J}}{dt}$, using eq. (2.1) and eq. (2.3) one obtains the equations of motion of a single dipole

$$\begin{cases} \frac{d\mathbf{S}}{dt} = -\gamma_e \mathbf{S} \times \mathbf{H_0} = \gamma_e \mathbf{H_0} \times \mathbf{S} \\ \frac{d\boldsymbol{\mu}}{dt} = -\gamma_e \boldsymbol{\mu} \times \mathbf{H_0} = \gamma_e \mathbf{H_0} \times \boldsymbol{\mu} \end{cases} \tag{2.4}$$

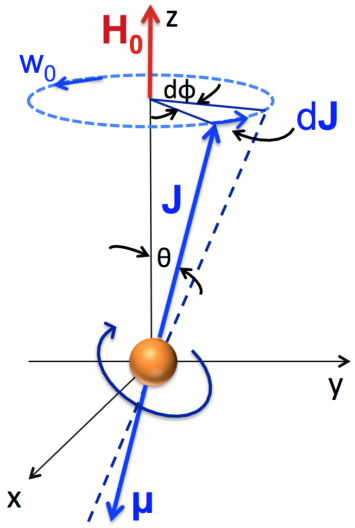

Figure 2.1: Spinning electron.

With reference to fig. 2.1, the angular velocity ω_0 can be written as

$$\frac{d\phi}{dt} = \frac{d\mathbf{S}}{dt}\frac{1}{S\sin(\theta)} \Rightarrow \frac{d\mathbf{S}}{dt} = \boldsymbol{\omega_0}, \times \mathbf{J} \tag{2.5}$$

where θ is the angle between $\mathbf{S}$ and $\boldsymbol{\omega_0}$. Then, eq. (2.4) and eq. (2.5) give

$$\boldsymbol{\omega_0} = \gamma_e \mathbf{H_0} \equiv \omega_L, \tag{2.6}$$

which is the natural precession frequency of a magnetic dipole in a constant magnetic field, also known as Larmor frequency. It is noteworthy that the precession frequency of the magnetization in a constant magnetic field is determined by the field strength, as in eq. (2.6). Since the magnetization of a medium with magnetically aligned spins is $\mathbf{M} = N\boldsymbol{\mu}$ where N is the number of unbalanced spins per unit volume, the second eq. of the system (2.4) becomes the equation of motion for the magnetization

$$\frac{d\mathbf{M}}{dt} = -\gamma_e \mathbf{M} \times \mathbf{H_0}. \tag{2.7}$$

2.1.1 Damping and resonance

The electronic magnetic moments in a medium spiral in due to damping phenomena until the magnetization reaches the equilibrium position along the static magnetic field direction. Damping can be considered as caused by the emitted magnetic dipole radiation, or by the material spin-spin and spin-lattice relaxation mechanisms. There are various phenomenological approaches to descibe the dynamics of the magnetization in presence of damping and small magnetizations. Here we present two possible forms, the Bloch-Bloembergen (B-B) [7], and Landau-Lifshitz-Gilbert (L-L-G) equations. The B-B equations for a magnetic material in a constant magnetic field H_0 in the z direction, are given by [8]

$$\frac{dM_{x,y}}{dt} = \gamma_e(\mathbf{M}\times\mathbf{H})_{x,y} - \frac{M_{x,y}}{\tau_2} - \frac{M_{x,yM_z}}{M_0\tau_r} \tag{2.8}$$

$$\frac{dM_z}{dt} = \gamma_e(\mathbf{M}\times\mathbf{H})_z - \frac{M_0 - M_z}{\tau_1} - \frac{M_x^2 + M_y^2}{M_0\tau_r}\,, \tag{2.9}$$

where the transverse components $H_{x,y}$ are related to the $dM_{x,y}/dt$ by geometrical factors, $\tau_{1,2}$ are the longitudinal (spin-lattice) and transverse (spin-spin) relaxation times, M_0 is the static magnetization directed along the z-axis, and τ_r is the radiation damping time.
The L-L form is given by

$$\frac{d\mathbf{M}}{dt} = \gamma_e(\mathbf{M}\times\mathbf{H_0}) - k_r\frac{(\mathbf{H_0}\cdot\mathbf{M})\mathbf{M}}{M^2} - \mathbf{H_0}\,. \tag{2.10}$$

In the second term of the equation, k_r is the phenomenological damping parameter, which is inversely proportional to the radiation damping time [10]. It can be expressed as

$$k_r = \alpha M\gamma_e\,, \tag{2.11}$$

where α is a dimensionless constant. Considering that $\mathbf{M}\cdot\mathbf{M} = M^2$ and applying the vector identity $\mathbf{a}\times(\mathbf{b}\times\mathbf{c}) = \mathbf{b}(\mathbf{a}\cdot\mathbf{c}) - \mathbf{c}(\mathbf{a}\cdot\mathbf{b})$, eq. (2.10) becomes

$$\frac{d\mathbf{M}}{dt} = \gamma_e(\mathbf{M}\times\mathbf{H_0}) - \frac{\lambda}{M^2}[\mathbf{M}\times(\mathbf{M}\times\mathbf{H})]\,. \tag{2.12}$$

The damping term in eq. (2.12) is clearly expressed as a vectorial contribution perpendicular to $\mathbf{M}$, and thus affects only the precessional angle, leaving the magnitude M constant (see fig. 2.2).

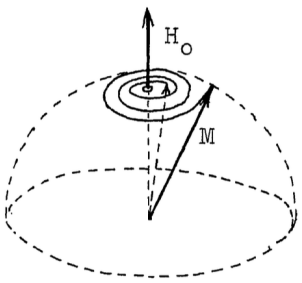

Figure 2.2: Magnetic damping.

Therefore, the damping factor in the magnetization precession can be controlled by the application of an oscillating field $\mathbf{h_{rf}}$ in the plane perpendicular to the constant field $\mathbf{H_0}$. If the frequency of $\mathbf{h_{rf}}$ is equal to the natural precessing frequency $f_L = \omega_L/2\pi$ of the system, the radiofrequency field can drive the magnetic resonance, the damping term can then be overcome and the precessional angle grows in

amplitude. In this resonant regime, the energy of the $\mathbf{h_{rf}}$ field is absorbed by the spinning electrons, causing the electron spin to flip between the two Zeeman sublevels. The quantity of energy absorbed depends on the field strength and is limited to a maximum, defined by the point when further increase in θ is prevented by damping. If the frequency of $\mathbf{h_{rf}}$ is not exactly equal to w_0, but differs from it by a small detuning value, frequency beats will appear in the precessional dynamics (fig. 2.6). If the detuning is too large, no compensation of the damping factor occurs, and the dynamics is described by an exponential decay.

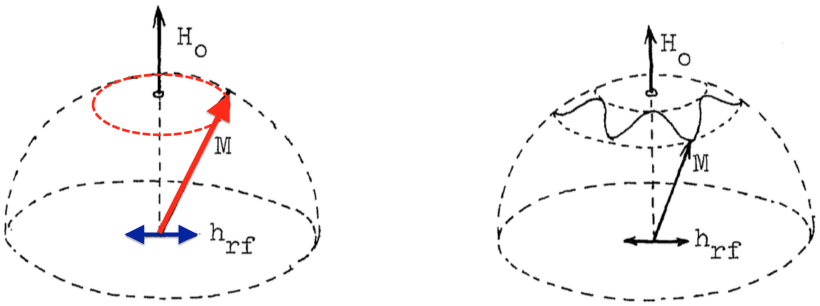

Figure 2.3: Left, precession of the magnetization vector when an oscillating field at frequency $f = f_L$ is applied. **Right**, frequency beats in the magnetization dynamics when $f \neq f_L$.

2.1.2 Line broadening

One of the advantages of using ferromagnets for magnetic resonance experiments is the very narrow linewidth, compared to the case of paramagnetic materials.
The most important cause of line broadening in a rigid lattice of magnetic dipoles is usually the magnetic dipolar interaction, which has a dominant role in paramagnetic media (or impurities), but is suppressed by the strong exchange coupling between electrons in ferromagnets [11]. Due to exchange coupling, the linewidth decreases, giving rise to an effect known as *exchange narrowing*. The effect can be explained in analogy with another phenomenon, the *motional narrowing*, which regards line drop for nuclei in rapid relative movement. In this case, diffusion resembles a random walk as atoms jump from one crystal site to the other.
Because of this rapid motion, the local field seen by a given spin fluctates rapidly in time, with a characteristic period τ. One can show that the resulting linewidth is $\Delta\omega = (\Delta\omega)_0^2\tau$, where $(\Delta\omega)_0 = \gamma_e \Delta B$ is the broadening in the rigid lattice, with ΔB the magnetic field seen by neighbour magnetic dipoles. The shorter is τ, the narrower is the resonance line. Motional narrowing is closely related to exchange narrowing, since the exchange frequency can be interpreted as a hopping frequency $1/\tau$. Given an exchange interaction J among nearest neighbour electron spins, the exchange frequency is $\omega_{ex} = J/\hbar$, and the width of the resulting exchange-narrowed line is

$$(\Delta\omega)_{ex} = (\Delta\omega)_0^2/\omega_{ex}\,. \tag{2.13}$$

2.1.3 Radiated microwave field

During the precession of the magnetization, due to the considered damping effects, energy is dissipated into spin-spin interaction, phonons generation (spin-lattice interaction), and magnetic dipole radiation, with the latter being the most efficient channel of energy conversion. The spinning electrons emit a dipole field that oscillates at the system precessional frequency and decays exponentially with time if the damping is not compensated by means of an external field at frequency $f = f_L$.

Damping effects can be suppressed by enclosing the sample in a microwave resonator, in the well-known cavity-QED regime. While in free field the system relaxation time depends on the Larmor frequency as $\tau_r^{-1} \propto \omega_L^3$ [7], in a cavity it is possible to accomplish a regime in which it is only determined by the material properties. In particular, if the cavity mode frequency f_c coincides with the system Larmor frequency f_L, hybridization takes place, i.e. the system is described through two eigenfrequencies $\omega_\pm$, as described in detail in sec. 2.4. In this case, the relaxation time is given by

$$\bar{\tau} = (\frac{1}{\tau_c} + \frac{1}{\tau_2})^{-1}, \tag{2.14}$$

where τ_c is the characteristic dacay time of the cavity. The advantage of performing FMR measurements in cavity is therefore a damping factor which no more depends on the frequency, and is strongly reduced in the presence of materials characterized by long τ_2 (for example in YIG τ_2 can be as high as $\approx 1\,\mu$s).

The dipole radiation emitted in the cavity or in the free field is employed in this thesis as observable of the magnetization precession, to be studied both in the time and frequency domain.

2.2 Optical excitation of magnetization

As discussed in the previous section, the magnetization precession is sustained in a steady-state regime by the application of an oscillating microwave field supplied by an external generator. In the new method described in this thesis the microwave driving field is optically produced. A multi-GHz infrared laser delivers a train of pulses in the time domain whose spectrum is composed by several harmonics at $n\,f_R$, with f_R the repetition frequency of the pulses ($\approx$GHz). Any harmonic of the frequency comb, provided it is tuned to the Larmor frequency, can drive the magnetization through the non-linear opto-magnetic process, described in detail in this work (sec. 2.3).

2.2.1 Individual femtosecond pulses

The conventional way to optically induce a magnetization precession is by means of a pump ultrafast laser pulse, which produces variations of the material properties [12]. In this case the optical signal generates a transient DC field in the material. The laser light frequency is in the near ultraviolet, visible or near infrared spectrum, hence oscillates at frequencies of the order of $1 \div 100$ THz, while the typical ferromagnetic or ferrimagnetic resonance belongs to the microwave range (order of $0.1 \div 100$ GHz). Therefore, the time duration of the laser pulse is the only significative time parameter and defines the time range of the interaction. To induce the electron-spin precession, the pulse duration must be shorter than the period of the Larmor motion, and ultrafast laser pulses are indeed the perfect tool to achieve these time ranges, going even below the femtosecond duration and thus being able to investigate also faster phenomena. Furthermore, the high intensity fields carried by the ultrafast laser pulses exceed the internal fields of an atom $\approx 10^{11}$ V/m and can thus give access to the underlying interactions.

2.2.2 Multi-GigaHertz picosecond pulses

The alternative mechanism which will be used in this thesis to accomplish a coherent excitation of the magnetization precession consists in supplying trains of pulses repeated at the Larmor frequency of the system. The laser tecnique which suits the purpose is called *modelocking*, and allows for ultrashort pulses of high peak intensities to be generated at high repetition rates [25], [26].
The schematic set-up (fig. 2.5(a)) consists in a laser resonator with a gain and a loss element, which allows through an output coupler to partially transmit a small fraction of the intra-cavity energy. By

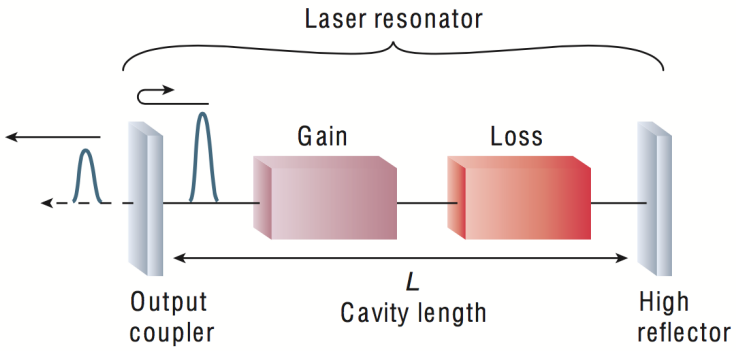

Figure 2.4: Passive mode-locking in a laser resonator.

establishing a fixed phase relationship between all of the longitudinal modes of the oscillator, laser light is collected in short pulses (fig. 2.5(a)), with a period given by $T_R = 2L/v_g$, where L is the laser cavity length and v_g is the group velocity associated to the peak of the pulse intensity.

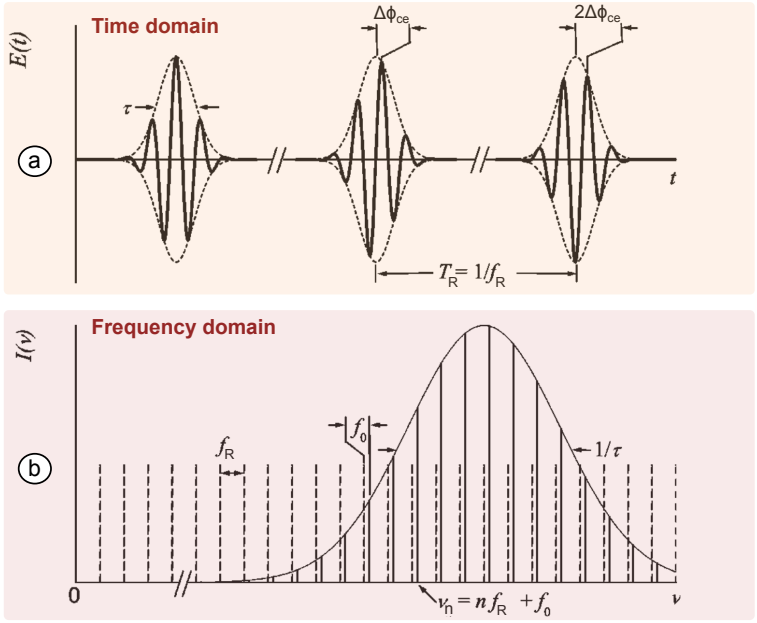

Figure 2.5: Modelocked laser pulses. (**a**) train of laser pulses in the time domain; the dashed line is the envelope function superimposed over the carrier wave, in bold line in the figure. The separation between the envelope peaks is the laser repetition rate; the carrier-envelope phase ϕ_{ce} evolves during propagation due to dispertion, causing a phase increment $\Delta\phi_{ce}$ for each pulse. (**b**) optical frequency comb; the Fourier transform of the envelope is superimposed over the optical frequencies ν_n.

The generated pulse train has a frequency spectrum that consists of a series of sharp, regularly spaced lines and is known as *microwave frequency comb* (fig. 2.5(b)). The connection between frequency and time domain can be understood with a simple model of the pulse, by decomposing it in the envolope function $A(t)$, which is superimposed on a continuous carrier wave of frequency w_c. The electric field of the pulse can therefore be expressed as $E(t) = A(t)e^{iw_c t}$. If only a single pulse is considered, its spectrum will be the Fourier transform of its envelope function, centered at the optical frequency w_c of the carrier, and its frequency width being inversely proportional to the time width of the envelope. For a train of identical, equally separated pulses instead, Fourier series expansion yields a comb of regularly spaced frequencies with the spacing being inversely proportional to the repetition rate of the laser T_R. The comb spectrum occurs because there are certain discrete frequencies at which the

interference is constructive, and these optical frequencies can be written as

$$\nu_n = n f_R + f_0 \tag{2.15}$$

In the equation n is a small number, f_R is the pulse repetition frequency, and f_0 is the comb offset. f_0 is caused by the phase shift ϕ_{ce} between the peak of the envelope and the closest peak of the carrier, which evolves with propagation due to dispersion in the medium. Its evolution results in a rigid shift of the frequencies at which the pulses add constructively. In particular, $f_0 \propto f_R \Delta\phi_{ce}$, where $\Delta\phi_{ce}$ is the increment of the carrier-envelope phase for each pulse.

2.3 Opto-magnetic non-linear phenomena

The physical mechanisms at the base of the optical control of the magnetization are nonlinear opto-magnetic processes which arise from the interaction of high intensity laser light with magnetically ordered materials.
The magnetization couples to the electromagnetic field of the laser light via the dielectric and susceptibility tensors, with higher order terms made important by the extremely high intensities. The effects of a pump laser pulse on a magnetic medium can be classified in the following classes [12]:

Thermal effects

[13], [14], [15], [16] The energy is pumped into the medium through absorption of photons. It is well known that the magnetization of a ferromagnetic or ferrimagnetic material decreases when heated. At temperatures above the Curie point the magnetic order is lost, and more generally, Curies's law describes the dependence to temperature of the magnetization as $\mathbf{M} = C\frac{\mathbf{B}}{T}$, where $\mathbf{B}$ is the magnetic field and C is the material specific Curie constant. Absorption of intense laser radiation can cause a temperature increase and thus lead to partial or total demagnetization. The underlying processes responsible of the phenomenon can be studied by conceptually separating the material into an electron, spin and lattice system, with respective temperatures T_e, T_s, T_l.

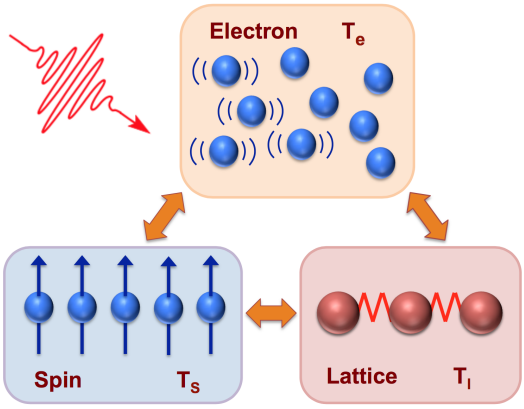

Figure 2.6: Conceptual illustration of interactions between electrons, spins and lattice, consequent to laser excitation. The T_i, $i = e, s, l$, are the temperature of the sub-systems.

In this model the change in magnetization corresponds to that of spin temperature $M = M(T_s)$. The interaction between the electric field of the laser pulse and the material mainly occurs via electronic excitations, since the optical transition mostly preserve the spin state. Subsequent interactions between the electron, spin and lattice systems lead to a rise of T_l and T_s until thermal equilibrium. The typical electron-lattice interaction is of the order of 1 ps, while the lattice-spin interaction in dielectrics

is of the order of few nanoseconds. The electron-spin interaction can be very short, down to 50 fs for ferromagnets, but in dielectric material is absent, due to the localized nature of their electronic states. The lifetime of such thermal effects depends on external parameters, as thermal conductivity or geometry of the sample.

Nonthermal photomagnetic effects

They involve the apsorption of pump photons, via electronic states that have direct influence on magnetic parameters as the magneto-crystalline anysotropy [17]. The process is istantaneous, growing with the time rise of the pulse. The magnetic parameters involved cause the motion of the magnetic moments according to the usual precessional behavior. The lifetime of this effect is the lifetime of the corresponding electronic states.

Nonthermal optomagnetic effects

They do not involve the absorption of pump photons, and are based on an optically coherent stimulated Raman scattering mechanism. In this case the spin-orbit coupling is responsible of the change in the magnetization and determines the time range of the process (≈ 20 fs for a typical 50 meV spin-orbit coupling) [17].

In practice, thermal effects can never be totally avoided and must be taken into consideration to some extent.
The magnetization dynamics was previously described by eq. (2.7) as function of the applied static field $\mathbf{H_0}$. Nevertheless, spins in a medium are not only affected by the external field, but also by internal contributions, like magnetocrystalline anysotropy, shape anysotropy, magnetic dipole interactions... [12]. These additional factors induce an effective magnetic field

$$\mathbf{H_{eff}} = \mathbf{H_0} + \mathbf{H_{ani}} + \mathbf{H_{dem}} + \dots, \tag{2.16}$$

where H_{ani} (anisotropy field) and H_{dem} (demagnetization field) are material dependent. Consequently, the precession of magnetic moments occurs around $\mathbf{H_{eff}}$. Therefore, the optical excitation of a magnetic material induces changes in the material-dependent field which affect the total $\mathbf{H_{eff}}$, resulting in an *optically-induced magnetization dynamics*. Equation (2.7) becomes

$$\frac{d\mathbf{M}}{dt} = \gamma_e(\mathbf{M} \times \mathbf{H_{eff}}) - \lambda \frac{(\mathbf{H_{eff}} \cdot \mathbf{M})\mathbf{M}}{M^2} - \mathbf{H_{eff}}. \tag{2.17}$$

Non-Linear polarization

In general, nonlinear optical effects are analyzed by considering the response of the dielectric material at the atomic level to the electromagnetic fields of an intense light beam. The propagation of a wave through a material produces changes in the spatial and temporal distribution of electrical charges as the electrons and atoms react to the electromagnetic fields of the wave. This perturbation creates electric dipoles whose macroscopic manifestation is the polarization. For small field strengths this polarization is proportional to the electric field. For stronger optical fields, higher orders terms become non-negligible and should be taken into account.
In a given material, the induced polarization per unit volume $\mathbf{P}$ can be derived from the expansion in terms proportional to one or more powers of electric field $\mathbf{E}$ and magnetic fielfd $\mathbf{H}$ (magnetic multipole effects). The polarization density can be expressed as $\mathbf{P}(\mathbf{r},t) = \mathbb{R}[\mathbf{P}_\omega e^{-i\omega t}]$, with the components of $\mathbf{P}_\omega$ given by

$$P^i_\omega = \varepsilon_0[\chi_{ij}E^j_\omega + \chi_{ijk}E^j_\omega H^k_\omega + \chi_{ijkl}E^j_\omega H^k_\omega H^l_\omega + \dots], \tag{2.18}$$

where ε_0 is the dielectric constant in the vacuum, and χ is the magneto-optical susceptibility multi-rank tensor. In particular, the multipole magnetic terms are negligible compared to the high intensity electric fields. Therefore, considering the expansion at the $O(H^2)$ order, it is possible to derive two important opto-magnetic effects introduced by the second term of the right-hand side of eq. 2.18, namely the Faraday effect and the inverse Faraday effect (IFE). For crystals invariant under time reversal, through permutation simmetries considerations of the χ operator, one obtains the following expressions for the magnetic dipole polarizations [18]:

$$P_i(\omega_2+\omega_1) = \chi_{ijk} E_j(\omega_2) H_k(\omega_1) \tag{2.19}$$
$$P_i(\omega_2-\omega_1) = \chi^*_{jik} E_j(\omega_2) H^*_k(\omega_1)\,. \tag{2.20}$$

The consequent expression for the magnetization yields:

$$M_k(\omega_1) = \chi^*_{ijk}\left[\, E_i(\omega_2+\omega_1)E^*_j(\omega_2) + E_i(\omega_2)E^*_j(\omega_2-\omega_1)\,\right]. \tag{2.21}$$

In the limit $\omega_1 \longrightarrow 0$, eqs. (2.19) describe the *Farday Effect*

$$\mathbf{P}(\omega_2) = i\,|\chi_{1,2,3}|\,\mathbf{E}(\omega_2)\times[\,\mathbf{H_0}+\mathbf{H_0}^*\,], \tag{2.22}$$

where one can show that $\chi_{1,2,3}$ are the only non-zero elements of the operator χ for an isotropic material, invariant under time reversal, and where the subcript stands for no equal indices. Being eq. 2.22 linear in the electric as well in the magnetic field, it introduces a birefringence for circularly polarized light, causing the polarization ellipses of the propagating light to gyrate around the direction of the static magnetic field H_0 [19]. This effect is also known as Faraday effect, and demonstrates that a magnetically ordered medium can indeed affect photons and change the polarization of light.

Inverse Faraday effect

For the symmetry properties of the electromagnetic field, also photons can affect the magnetization. In fact, in zero applied magnetic field, and with circularly polarized optical field propagating in the k direction, eq. (2.21) shows that there is a k-component of magnetization at zero frequency

$$\mathbf{M_k}(0) = \pm 2\,|\chi_{1,2,3}|\,[\mathbf{E}(\omega_2)\times\mathbf{E}^*(\omega_2)] = \pm 2\,|\chi_{1,2,3}|\,|\mathbf{E}|^2\,. \tag{2.23}$$

This is the inverse Faraday effect, and shows that circularly polarized light in a magnetic medium acts as an effective magnetic field which involves the generation of a magnetic excitation, as demonstrated by several theoretical approaches [18], [20], [21], and confirmed in different experimental conditions [12], [22] after the pioneering work of Bell and Bloom on alkali metal vapors [9].
Thus, in a thermodynamical approach, the effect of light on spins in a magnetically ordered material can be described by the L-L-G equation (2.10) or by the B-B form (2.8), where the alternate magnetic field is generated by light via the IFE. In our experimental framework, the frequency ω_2 is the electromagnetic frequency of the laser light (of the order of 100 THz), while $\omega_1 \longrightarrow 0$ is the laser pulses repetition frequency f_R (eq. 2.15).

Circular and linear polarization in the IFE

The generation of the quasi-static axial magnetic field involved in the IFE, has mainly been associated with circularly polarized radiation propagating through an unmagnetized plasma (zero applied magnetic field), as described above. Nonetheless, the IFE can also occur with *linearly polarized* radiation.
Owing to the strong anisotropy of the magnetic susceptibility of YIG, the non-zero terms of the third-rank tensor χ do not simplify to $\chi_{1,2,3}$ as in 2.22. Consequently, the allowed solutions of eq.

(2.23) are not limited to circularly polarized light beams, and include also linearly polarized pulses. Furthermore, the magnetization vector **M** is not expected to be parallel to the wave vector k as is the case for IF in isotropic medium and circularly polarized light.

2.4 Dynamics of coupled oscillators

In this thesis, the optically driven precession of the magnetization dynamics is demonstrated both in free field and in a cavity. In this section we describe in detail the hybridization that takes place in the latter through a model of two simple coupled harmonic oscillators (CHOs) whose dynamics is studied in terms of energy exchange and losses [41].

2.4.1 CHOs Model

Coupled dissipative systems display two regimes of behaviour known as *weak coupling* and *strong coupling*, a distinction that is necessary to determine whether the coupled constituents of the system merely perturb each other, or their mutual influence is so strong that their individuality is lost.
In the model we have used, the forced oscillators are allowed to exchange energy via a coupling spring, with stiffness constant K, and each of them loses energy to their surroundings via friction terms γ_i, as illustrated in fig. 2.7. Each oscillator is identified by:

- the uncoupled eigenfrequency $\omega_j = \sqrt{k_j/m_j}$,
- the coupling rate $\Omega = \sqrt{K/m}$,
- the stiffness constant k_j of the spring with fixed extremity,
- the oscillator mass m_j (m is the effective mass).

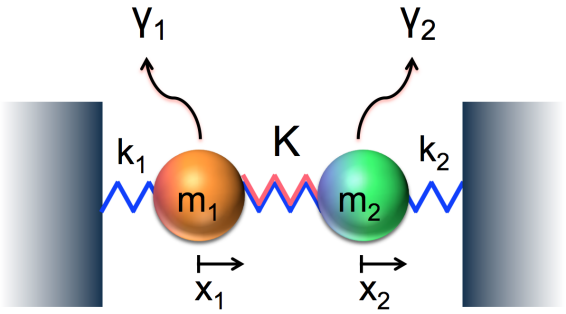

Figure 2.7: Pair of coupled harmonic oscillators; m_1, m_2 are the respective masses, k_1, k_2 the stiffness constants of the springs at the extremities, γ_1, γ_2 the loss rates, x_1, x_2 the displacements from equilibrium, and K the stiffness constant of the coupling string.

There are various contexts where the distinction between weak and strong coupling can be respectively identified, which lead to the following definitions:

- ✯ the dynamics is governed by exponential decay or energy exchange cycles;
- ✯ the spectrum of the driven system displays a single resonance or two split peaks;
- ✯ the eigenfrequencies of the CHOs cross or anti-cross, as the frequency difference between the oscillators transits through zero.

In general the two widespread criteria [42, 43, 44, 45] to distinguish between weak and strong coupling are:

- ☆ Strong coupling occurs when the energy exchange rate exceeds *all* the loss rates, or alternatively, when the frequency splitting ($\propto$ coupling strength) is larger than the *sum* of the linewidths ($\propto$ loss rates). In fact, when the driving force excites both the eigenmodes of the coupled system, two split peaks arise in the spectrum. In practice, this criterion relies on whether the two split peaks are visible in the spectrum (strong coupling) or not (weak coupling).
- ☆ Strong coupling occurs when the energy exchange rates exceed the *difference* of the loss rates, rather than their individual values or sum. This second criterion is less used and less suited to representation than the first, in fact it implies that two identical oscillators with arbitrarily high losses are strongly coupled for any non-zero energy exchange rate. However, if the energy exchange rate is much less than the loss rates, the strongly coupled system does not exhibit energy exchange cycles or split peaks in the spectrum.

CHO dynamics

The equations of motions for two damped CHOs ($j = 1,2$), expressed in terms of the displacement x_j from equilibrium, and in absence of a driving force, are

$$\begin{aligned} \ddot{x}_1 + \gamma_1 \dot{x}_1 + \omega_1^2 x_1 - \Omega^2 x_2 = 0\,, \\ \ddot{x}_2 + \gamma_2 \dot{x}_2 + \omega_2^2 x_2 - \Omega^2 x_1 = 0. \end{aligned} \tag{2.24}$$

Let us consider two identical oscillators, thus $m_1 = m_2 = m$, $\omega_1 = \omega_2 = \omega_0$, $k_1 = k_2 = k$, $\gamma_1 = \gamma_2 = \gamma$, and the particular case of underdamped oscillators ($\gamma/2 < \omega 0$), which is useful to distinguish between weak and strong coupling. The two second order differential eqs. (2.24) can be reduced to four first order differential equations using the following representation

$$\begin{aligned} q_1 &= x_1\,, \\ q_2 &= \dot{x}_1\,, \\ q_3 &= x_2\,, \\ q_4 &= \dot{x}_2\,. \end{aligned} \tag{2.25}$$

The vector $\mathbf{q}$ defined above evolves in time following the matrix of differential equations:

$$\begin{bmatrix} \dot{q}_1 \\ \dot{q}_2 \\ \dot{q}_3 \\ \dot{q}_4 \end{bmatrix} = \begin{bmatrix} 0 & 1 & 0 & 0 \\ -\omega_1^2 & -\gamma_1 & \Omega^2 & 0 \\ 0 & 0 & 0 & 1 \\ \Omega^2 & 0 & -\omega_2^2 & -\gamma_2 \end{bmatrix} \begin{bmatrix} q_1 \\ q_2 \\ q_3 \\ q_4 \end{bmatrix}. \tag{2.26}$$

The total energy of the oscillators can therefore be expressed as $E_1 = T_1 + V_1 = \frac{mq_2^2}{2} + \frac{kq_1^2}{2}$ and $E_2 = T_2 + V_2 = \frac{mq_4^2}{2} + \frac{kq_3^2}{2}$, where $\mathbf{q}$ is the solution of the Cauchy problem of the previous linear system [1].
A meaningful observable of the system is the dissipated power, which is indeed the physical quantity we have measured for the analysis of our system. It can be calculated by introducing in eq. (2.24) the action of a driven harmonic force of frequency ω_d, on the first oscillator only, as first case. Representing the displacement variable as $x_j(t) = x_j^0(0)e^{-i\omega_d t}$ and the force as $Fe^{-i\omega_d t}$, the dynamics of the driven dissipative CHOs is described by the following matrix

$$\begin{bmatrix} \omega_0^2 - \omega_d^2 - i\gamma_1\omega_d & -\Omega^2 \\ -\Omega^2 & \omega_0^2 - \omega^2 -_d i\gamma_2\omega_d \end{bmatrix} \begin{bmatrix} x_1 \\ x_2 \end{bmatrix} = \begin{bmatrix} Fe^{-i\omega_d t} \\ 0 \end{bmatrix} \tag{2.27}$$

[1] Representing the linear system with the equality $\dot{q} = Aq$, if λ_j and v_j are the eigenvalues and respective eigenvectors of A, then the linear independent solutions of the linear system are $\phi_j(t) = e^{\lambda_j t} v_j$. Being $\Phi(t)$ the matrix built from $\phi_j(t)$ as columns, the solution of the Cauchy problem is $y(t) = e^{tA} y_0$, where $e^{tA} = \Phi(t)\Phi(0)^{-1}$ and y_0 is the initial condition.

The power dissipated by the j^{th} oscillator at the driven frequency ω_d, is $P_j = \omega_d^2 \gamma_j |x_j(\omega_d)|^2$, where $x_j(t)$ are the components of the vector below

$$\begin{bmatrix} x_1 \\ x_2 \end{bmatrix} = \frac{1}{|A|} \begin{bmatrix} \omega_0^2 - \omega_d^2 - i\gamma_2\omega_d & \Omega^2 \\ \Omega^2 & \omega_0^2 - \omega_d^2 - i\gamma_1\omega_d \end{bmatrix} \begin{bmatrix} Fe^{-i\omega t} \\ 0 \end{bmatrix}, \tag{2.28}$$

and where, formalizing eq. (2.27) as $Ax = F$, $|A| = (w_0^2 - w_d^2 - iw_d\gamma_1)(w_0^2 - w_d^2 - iw_d\gamma_2) - \Omega^4$.
The total energy $T_{1,2} + V_{1,2}$ and total power P_{tot} are plotted respectively on the top and on the bottom of fig. 2.8. The total energy is function of the dimensionless time $\omega_0 t/\gamma$ (where ω_0 is the eigenfrequency of the uncoupled oscillators and γ their loss rate), while the total power is function of the driven frequency ω_d normalized to the eigenfrequency of the uncoupled oscillators, and both functions are normalized to the unity (in the upper spectra the normalization factor is chosen as to bring $Max(T_1)$ to the unity). The four cases refer to four different values of the ratio $R = \Omega^2/\omega_0\gamma$.

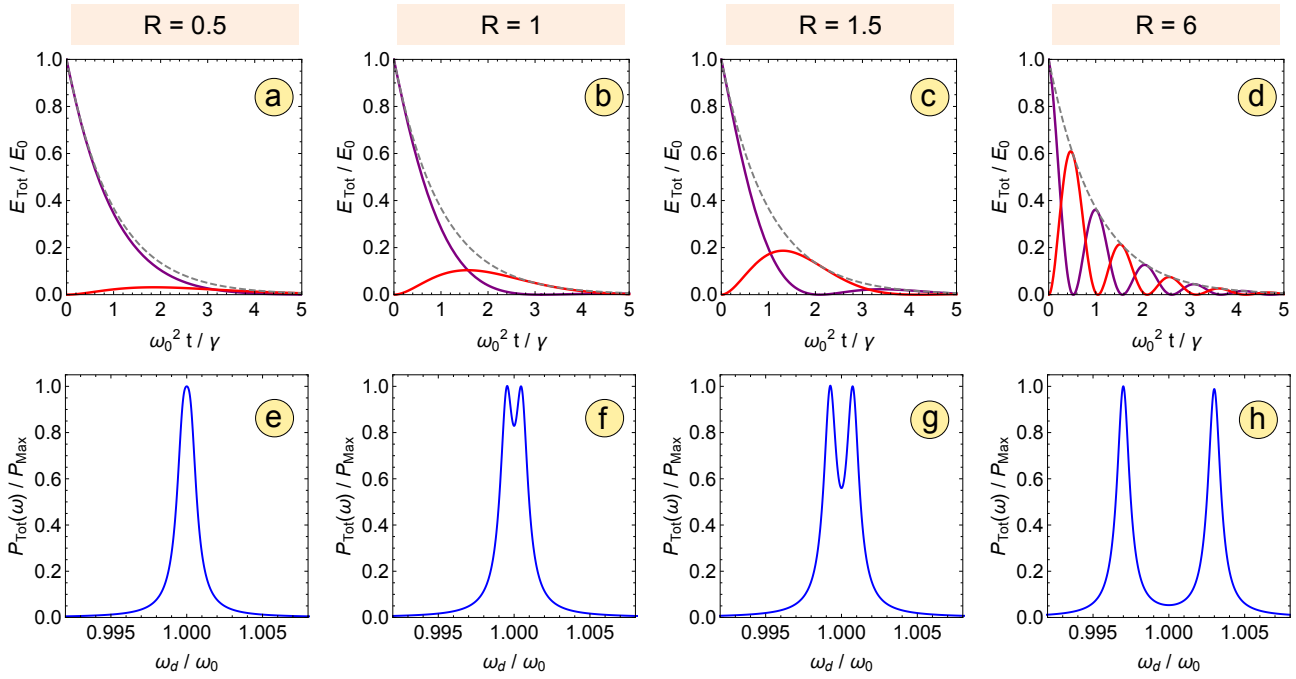

Figure 2.8: Energy cycles and dissipated power of a pair of CHOs, for four values of the ratio $R = \Omega^2/w_0\gamma$. **a**, **b**, **c**, **d**, time evolution of total normalized energy (kinetic plus potential), where γ and w_0 are the loss rates and eigenfrequencies of the uncoupled oscillators. The purple line is the energy stored in the driven oscillator, the red line is the energy in the second oscillator, the grey dashed line is the dynamics for the case $\Omega = 0$ ($R = 0$), corresponding to an exponential decay $e^{-2\gamma t}$ of the energy stored in the driven oscillator. **e**, **f**, **g**, **h**, dissipated power of both the oscillators when only one oscillator is driven by a harmonic force oscillating at frequency w_d.

The values of the constant parameters are reported in the following table

$\omega_0\,[Hz]$	$\gamma\,[Hz]$	$F\,[m/s^2]$	$x_1^0\,[m]$	$\dot{x}_1^0\,[m/s]$	$x_2^0\,[m]$	$\dot{x}_2^0\,[m/s]$
1	0.001	0.1	$\sqrt{2}$	0	0	0

Table 2.1: System parameters of the CHOs.

where x_1^0, $\dot{x}_1^0$, x_2^0 and $\dot{x}_2^0$ are the initial conditions of the oscillators. With reference to fig. 2.8, energy cycles and dissipated power will be described below for the different cases.

Energy cycles

When $R < 1$, loss dominates over energy exchange and the system is weakly coupled. An example is shown in fig. 2.8(a), where the energy stored in the driven oscillator (purple line) is dissipated before it can be transferred to the second oscillator (red line). The extreme case $\Omega = 0$ is qualitatively similar, displaying an exponential decay $e^{-\gamma t}$ of the energy in the driven oscillator (grey dashed line). Therefore, the weak coupling simply exerts a perturbative effect on the exponential energy decay of the excited CHO.
The system enters the other regime when $R > 1$. Fig. 2.8(b) shows the case $R = 1$, where a single cycle of energy exchange is barely induced. The exchange becomes more efficient with the growing of R (fig. 2.8(c)), until multiple cycles can be observed (fig. 2.8(d)). The observation of cycles illustrates that the CHOs transfer energy between them faster than they each dissipate energy, and this effect is therefore associated with the strong coupling regime.

Dissipated power

According to the definition presented at the beginning of the chapter and based on energy cycles, the transition between weak and strong coupling is represented by the splitting of a single resonance frequency into two resonances. This effect is the well-known *Rabi splitting*. On the bottom of fig. 2.8, the spectra show an increasing splitting as the coupling strength becomes stronger, while the two peaks are centered on the eigenfrequency of the identical oscillators independently on the coupling. From the experimental point of view a critical parameter is the oscillator mode linewidth, which must be sufficiently narrow to observe the coupling.

Another signifactive feature of strong coupling is the *avoided resonance crossing* (ARC), which refers to the approach and subsequent repulsion of two resonances in the frequency domain, as the uncoupled eigenfrequency detuning $\delta = \omega_1 - \omega_2$ is varied. The phenomenon is illustrated in fig. 2.9 where the dissipated power is calculated as a function of the adimensional variables ω/ω_0 and δ/γ.

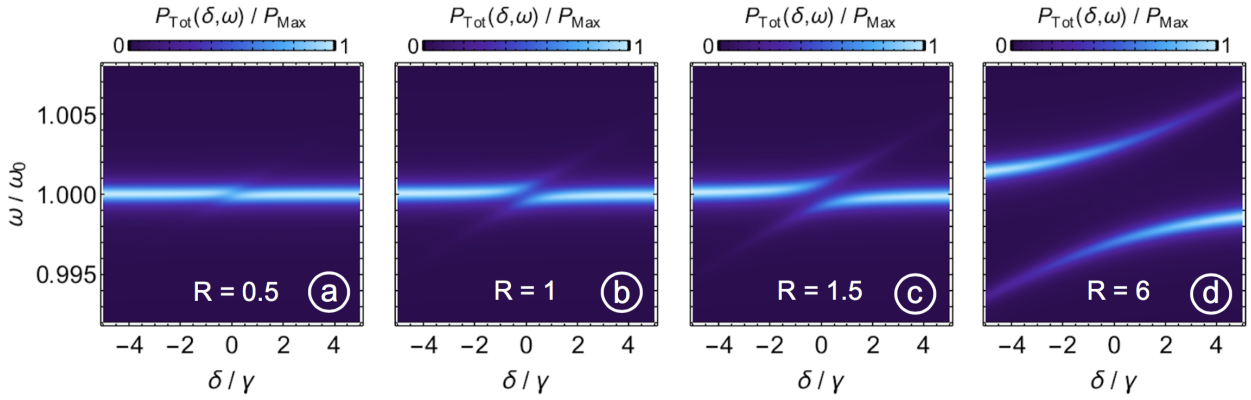

Figure 2.9: Dissipated power of a pair of CHOs when one oscillator is driven by a harmonic force. The dissipated power is normalized to the resonance value and is function of the adimensional quantities ω/ω_0 and δ/γ, where the variable ω is the frequency of the driving force, $\omega_0 = \omega_1$, $\delta = \omega_1 - \omega_2$ is the uncoupled eigenfrequency detuning and γ is the loss rates of the oscillators. **a**, **b**, **c**, **d**, the spectra are displayed for four values of the ratio $R = \Omega^2/\omega_0\gamma$.

The system parameters are the same of table 2.1, and $\omega_0 = \omega_1$ for convenience, while the variable w is the the harmonic force frequency. The colour maps in figure 2.9 are displayed for different values of the parameter $R = \Omega^2/\omega_0\gamma$. The two anticrossing resonances at $\delta = 0$ constitute the ARC, and their frequency splitting at $\delta = 0$ is known as *Rabi splitting*. In the weak coupling regime the ARC is barely

visible (fig. 2.9(a)) while in the strong coupling regime it clearly appears (fig. 2.9(d)). In the weak coupling regime a frequency detuning of one linewidth (γ) is sufficient to destroy the coupling, hence the driven oscillator behaves independently. Viceversa, in the strong coupling regime the influence of the second oscillator endures the detuning.

CHAPTER 3

Properties of YIG Samples

The magnetic properties of ferromagnetic materials have been vastly studied due to their application in microwave technologies, mainly as filters or resonators [27]. There are a variety of single-crystal materials that have possible use as ferromagnetic resonators, as for example Yittrium-Iron garnet (YIG), Gallium-substituted YIG, Lithium ferrite or Barium ferrite. Among all, the YIG material has proved to be the most useful due to its unique properties for FMR. It has the narrowest known linewidth of ferromagnetic resonance lowest spin-wave damping, and high unpaired electron density. In general, among the several parameters that characterize ferromagnetic (and ferrimagnetic) resonators, the most important are [27]:

- The saturation magnetization M_s
- The resonance linewidth Δf, or the Q factor, defined as $f/\Delta f$
- The anisotropy field constant K_l/M_s
- The Curie temperature T_c.

In general, the peculiar features of ferromagnetic (and ferrimagnetic) resonance include the following facts[11]:

- ✦ The shape of the specimen plays an important role since it influences the intensity of the demagnetizing internal field [29], with consequences on the effective internal fiels, on the magnetization and on its precessional frequency.
- ✦ The suceptibility components are very large, in fact the magnetization of a ferromagnet in a given static field is considerably larger than in paramagnets in the same field.
- ✦ The strong exchange coupling between electrons tends to reduce the contribution of dipolar interactions to the resonance line width, so that it can result very sharp under proper conditions.

The saturation magnetization M_s is a function of the number of unpaired electron spins in the material per unit volume, and refers to the maximum value that the magnetization can reach in an external applied magnetic field.
The resonance line width Δf is the full width half maximum of the corresponding peak in the emission frequency spectrum of the polarized material. The line width depends on various experimental parameters, as the material itself, the shape and the surface of the sample. An important condition

for the line width to be narrow, then for the Q factor to be high, is a uniform internal magnetic field, and the optimal shape for this situation is a spheroidal or ellipsoidal with highly polished surface (see subsec. 3.0.5).
The first-order anisotropy field constant K_l/M_s depends on the intrinsic lattice structure of the crystal material, which makes it easier to magnetize along some preferential crystal axes. Consequently, the FMR frequency is influenced by the orientation of the crystal axes with the applied static field H_0 (see subsec. 3.0.6). The second-order anisotropy field constant can instead be neglected since it is much smaller than the first-order one.
The Curie temperature T_c is the value at which the saturation magnetization drops to zero.
Some typical reference values of the previous parameters for YIG are reported below

$4\pi M_s\,[10^3\,A/m]$	$4\pi K_l/M_s\,[10^3\,A/m]$	$4\pi\Delta H\,[10^3\,A/m]$	$T_c\,[K]$
1750	−43	0.22	559

Table 3.1: FMR parameters for YIG.

The first three parameters in the table were measured at room temperature [27]. The parameter ΔH is a different definition for resonance line width, being the field width of the resonance peak as the signal frequency is held constant and the applied static field is varied. The resonance line width can vary significantly from sample to sample depending on the purity of the crystal structure, while M_s, K_l/M_s and T_c are physical constants for a given material, but M_s and K_l/M_s do vary considerably with temperature. The variation of the anysotropy constant, as of the magnetization saturation M_s, is significant when the temperature change is of the order of 100 K [31]. In this thesis the experimental set-up is kept at room temperature with no relevant changes, therefore the dependence on temperature will be neglected.

3.0.1 Structural Properties

Garnets belong to a class of dielectric, magnetic minerals with a characteristic crystal structure but with a great diversity in chemical composition. The name is derived from 'granum', meaning grain. In the 1950s, synthetically made garnets with ferrimagnetic ordering were found to exhibit a wide range of magnetic phenomena, causing them to be studied intensively over the past decades [33], [34]. They have served as ideal model systems for both experimental and theoretical studies of magnetic phenomena. Their magnetic properties derive from the structure of the particular ions in the crystal.
The chemical composition of YIG is $\{Y_3\}[Fe_2](Fe_3)O_{12}$ and its crystal structure is cubic. In the chemical formula the different brackets are used to indicate the three different coordinations of the cations with respect to oxygen in the crystal. The large yttrium Y^{3+} ions are located in the dodecahedral positions (denoted { }) where they are surrounded by eight O^{2-} ions at the corners of a dodecahedron. The Fe^{3+} ions with smaller ionic radii are located in octahedral sites (denoted [ ]) with six nearest oxygen ions as neighbors forming an octahedron. Trivalent iron ions are also found in tetrahedral sites (denoted ( )), surrounded by four oxygen ions which occupy the corners of a stretched cube. In a unit cell there are 24 of the large dodecahedral sites, 16 of the octahedral sites, and 24 of the smallest sites with tetrahedral point group symmetry.
A unit cell of YIG contains 8 formula units and has a lattice constant of 12.376. It is a rather loose structure with a volume of 236.9A^3 per formula unit.

3.0.2 Magnetic Properties

The fundamental magnetic properties of YIG derive from the magnetic ions, principally Fe^{3+}, and their relationship to the surrounding oxygen ions.

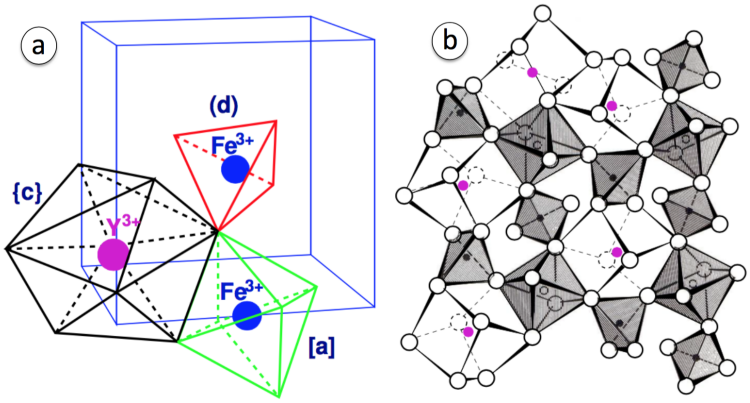

Figure 3.1: (**a**) The garnet structure, adapted from [35]. Arrangement of the $[a]$, $\{c\}$ and (d)-sites at the centers of octahedra, dodecahedra and tetrahedra, respectively. The cube represents one octant of the unit cell. ((**b**)) Spatial connection of oxygen polyhedra in YIG, adapted from [36]. The large open circles represent oxygen anions and the small circles represent cations.

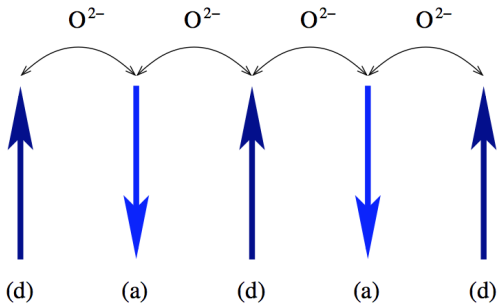

Figure 3.2: Illustration of the antiferromagnetic superexchange coupling of the magnetic moments of Fe^{3+} ions on tetrahedral (d) and octahedral (a) sites mediated by O^{2-}.

The oxygen ions influence the electronic configuration of the enclosed iron ions and mediate a superexchange interaction between the iron on octahedral (a) and tetrahe- dral (d) sites. The magnetic moments of Fe^{3+} ions in dfferent crystallographic sites are antiferromagnetically coupled (fig. 3.2).

3.0.3 Optical and Magneto-Optical Properties

YIG has a band gap of about 2.9 eV and is highly transparent ($\alpha << 0.03\,\mathrm{cm}^{-1}$) to light in the infrared wavelength region $[1.5 \div 5]\,\mu$m [32], [33] (fig.). At longer wavelengths absorption is caused by lattice vibrations, while at shorter wavelengths electronic transitions within the Fe^{3+} ion (crystal field transitions) and charge transfer transitions are responsible for the optical absorption.

In figure fig: absorption (b), the $1.550\,\mu$m-wavelength and the $1.064\,\mu$m-wavelength adopted in this thesis, correspond to ≈ 0.8 eV and ≈ 1.2 eV respectively. YIG and rare earth iron garnets exhibit strong magneto-optical Faraday and Kerr effects. The microscopic origin of these large effects are not fully understood, but they are believed to originate from the high-energy charge transfer optical transitions, with the effect extending down through the visible and the near infrared spectral regions [33]. In YIG, the contribution of the octahedral iron sublattice to the Faraday rotation is larger than that of the tetrahedral iron sublattice.

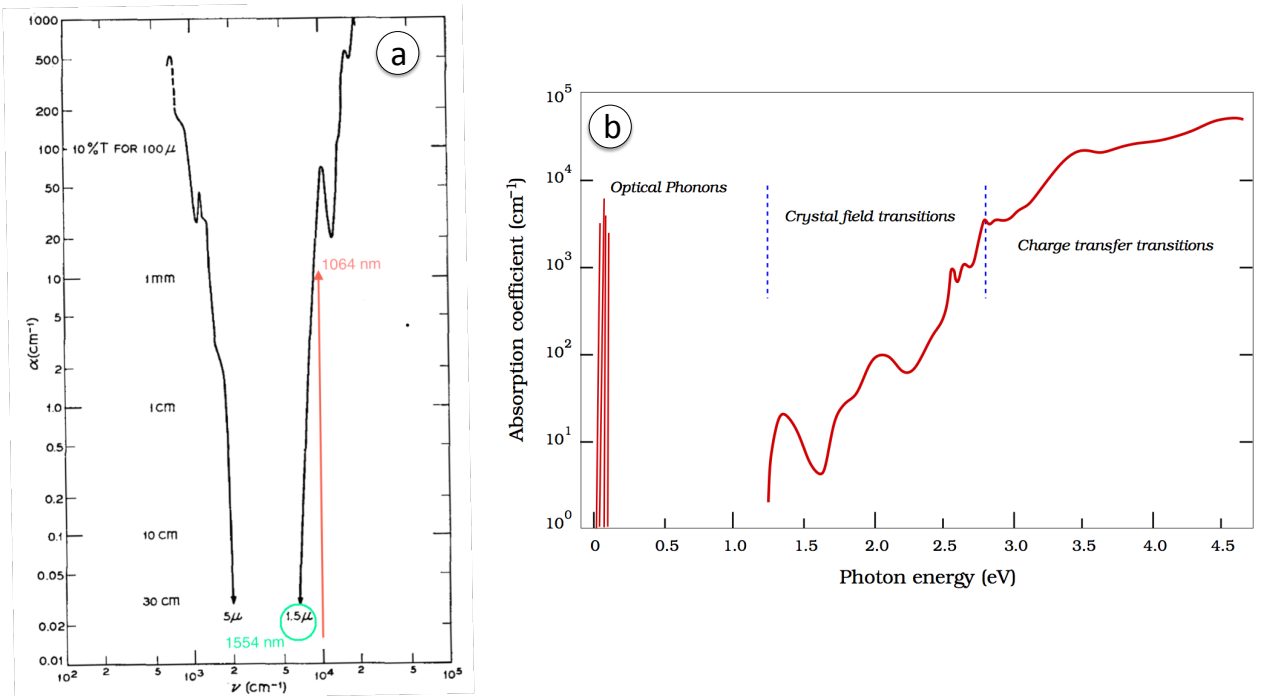

Figure 3.3: Optical absorption of YIG, in the frequency (**a**) and energy **b** domain.

3.0.4 Coupling Properties of the Magnetic Modes

YIG is considered the ideal material for ferromagnet-based hybrid systems [47], [48], [49], [4]. Although the coupling strength g_0 of an individual spin to the electromagnetic mode of a microwave resonator is small (typically 10 Hz for a superconducting resonator), the coupling of N spins is enhanced by the factor of $\sqrt{N}$. In general, ferromagnetic materials display the following advantages for the enhancement of coupling to electromagnetic modes [52]

- Their high spin density, such that for the same number of N spins the material volume can be considerably reduced compared to paramagnetic materials. The typical spin density in paramagnetic materials is of the order of $(10^{15} \div 10^{18}\,\mathrm{cm}^{-3})$, while in ferromagnet it is at least four orders greater in magnitude, or alternatively of the order of one spin per atom. Consequently, the coupling strength of exchange coupled systems is expected to be at least two orders of magnitude larger as compared to noninteracting spins. In ferromagnets, because of the strong exchange interaction in between, spins are perfectly ordered in the ground state, and the excitations are collective waves of small-angle spin precession. In a sample with finite dimensions, dipolar interaction dominates the long-wavelength limit, and the boundary condition at the surface defines rigid discrete modes called *magnetostatic modes*. In particular, the spatially uniform mode is called *Kittel mode*.

- Below the magnetic ordering temperature (Curie temperature) the system essentially is fully polarized, while uncoupled spin ensembles in paramagnetic centers undergo thermal polarization.

- Relaxation mechanisms are such that it is possible to simultaneously have high spin density and low damping. On the contrary, in diluted paramagnetic systems spin-spin interaction can cause dephasing and decoherence, thus higher spin densities allow stronger coupling with the elctromagnetic field but spin-spin interactions drastically shorten the coherence time.

In particular, YIG has very narrow linewidth, high quality fabrication possibilities, very low damping rate, and extremely high spin density ($\sim 10^{22}\,\mathrm{cm}^{-3}$). The contribution of magnetic dipole interactions

to the linewidth of spin excitations, which are dominant in paramagnetic impurities, is in this case suppressed by the strong exchange coupling between ferromagnetic electrons. Consequently the spin-spin interactions in YIG give rise to coherent modes which strongly couple with microwave photons.

3.0.5 Shape Effects and Uniform Modes

Compared to the Larmor frequency of a magnetic dipole in a constant magnetic field (eq. (2.6)), the resonant frequency of a ferrimagnet may differ from that expression because of topology and anysotropy factors.
Considering a specimen in the form of an ellipsoid with principal axis $a_x = a_y$, a_z parallel to the cartesian coordinates, and calling N_x, N_y, N_z the demagnetizing factors [30], the components of the internal magnetic field $\mathbf{B^i}$ can be expressed as follows [11]:

$$B^i_x = H_{0,x} - N_x M_x\,; \qquad B^i_y = H_{0,y} - N_x M_y\,; \qquad B^i_z = H_{0,z} - N_x M_z\,. \tag{3.1}$$

Substituting $\mathbf{B^i}$ in the equation (2.7) of motion for free spins, for an applied static field $H_0\hat{z}$ one obtains:

$$\begin{aligned} \frac{dM_x}{dt} &= \gamma_e(M_y B^i_z - M_z B^i_y) = \gamma_e[H_0 + (N_y - N_z)M_z]M_y\,; \\ \frac{dM_y}{dt} &= \gamma_e(M_z B^i_x - M_x B^i_z) = -\gamma_e[H_0 + (N_x - N_z)M_z]M_x\,]\,; \\ \frac{dM_z}{dt} &= \gamma_e[M_x M_y (N_x - N_y)]\,. \end{aligned} \tag{3.2}$$

where to first order one can consider $\frac{dM_z}{dt} = 0$, thus $M_z = M$. The non banal solutions of eq. (3.2), considering a time dependence $e^{-i\omega t}$, give the magnetic resonance frequency in an applied field H_0:

$$\omega_0^2 = \gamma^2[H_0 - (N_y - N_z)\mu_0 M][H_0 + (N_x - N_z)\mu_0 M] \tag{3.3}$$

where $\mu_0 M$ was substituted to M (with consequent redefinition of $N_{x,y,z}$), according to SI. The frequency ω_0 is known as frequency of the *uniform mode*, and refers to a uniform resonant dynamics where all the magnetic moments precess in phase with the same amplitude. Uniform modes can be pictured as uniform volume excitations, in distinction to magnons, for example, which are resonances arising from a difference in the anysotropy fields seen by the electron spins on the surface. For a spherical specimen, the demagnetizing factors are $N_x = N_y = N_z = \frac{1}{3}$ and eq. (3.3) returns eq. (2.7):

$$w_0 = \gamma H_0 \tag{3.4}$$

Considering other limiting cases of the elipsoid, the effect of shape on the resonant frequency becomes evident. For an infinitely thin rod parallel to $H_0\hat{z}$ the demagnetizing factors are $N_x = N_y = \frac{1}{2}$ and $N_z = 0$; for an infinitely thin disk lying in the zy plane one gets $N_x = 1$ and $N_y = N_z = 0$; for the same disk in the xy plane $N_x = N_y = 0$ and $N_z = 1$.
The shape of the specimen mainly employed in this work is a spherical YIG, being the most practical both for the uniformity factor and precision of fabrication.

3.0.6 Crystalline Anysotropy

The YIG material has a cubic crystal structure and therefore its three principal crystal axes are the $[100]$, $[110]$ and $[111]$ (fig. 3.4). For each cubic cell, there are three $[100]$, six $[110]$ and four $[111]$ axes, and their relative orientation with the applied external field $\mathbf{H_0}$ influences the resonant ferrimagnetic frequency. For a YIG material, the $[111]$ are known as *easy axes*, while the $[100]$ are *hard axes*. In fact, the expressions for the resonant frequency for a sphere of cubic crystal material, with the axis $[111]$ or $[100]$ respectively parallel to $\mathbf{H_0}$, yield [27]:

$$w_0 = \gamma(H_0 - \frac{4}{3}\frac{K_l}{M_s})$$
$$w_0 = \gamma(H_0 + 2\frac{K_l}{M_s}). \tag{3.5}$$

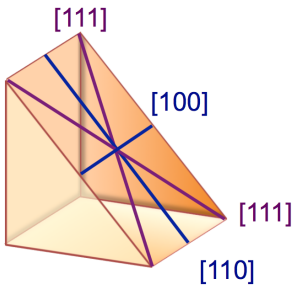

Figure 3.4: Principal axes of a cubic crystal structure.

Since the anisotropy field constant $\frac{K_l}{M_s}$ is negative for the YIG, resonance is achieved for a lower field strength if the easy axis is parallel to the field, and the difference in resonant frequency for the two cases is about 400 MHz.
In particular, in this thesis the working condition is with the [110] axis perpendicular to $\mathbf{H_0}$. In this case, the relation of the biasing field to the resonance frequency becomes

$$H_0 = \frac{w_0}{\gamma} - (2 - 35/8 sin^2(\theta))\frac{K_l}{M_s}, \tag{3.6}$$

where θ is the angle between H_0 and [100]. This means that while rotating the sphere around the [110] axis, the [100] or the [111] axis will be parallel to the field at different times, and consequently also the field strength required for reaching the resonance point will vary.

3.0.7 Dielectric Tensor of Anisotropic Magnetic Media

One of the fundamental magnetic quantities to be analyzed for a deeper understanding of opto-magnetic effects in anisotropic media (sec 2.2.1) is the electric permittivity tensor ε, which can be described as a measure of how an electric field affects a dielectric medium. The propagation of a magnetic field in the magnetic material can cause a change in ε with a resulting anysotropy of the three-dimensional tensor and complex off-diagonal elements, depending on the frequency ω of incident light. As a consequence, left- and right-rotating polarization travel at different speeds and several opto-magnetic effects emerge from the interaction of the radiation with the material. Magneto-optics can be described, from a macroscopic point of view, in terms of the effective magnetic tensor by setting the permeability $\mu = 1$ [28].
The definition of the dielectric tensor ε for an electric field of frequency w is

$$D_i(w) = \sum_{j=1}^{3} \varepsilon_{ij}(w) E_j(w), \quad i = 1, 2, 3 \tag{3.7}$$

where D is the displacement field, representing how the electric field influences the organization of electric charges inside the medium. Concerning with sinusoidally oscillating fields $\mathbf{D}, \mathbf{E} \propto e^{i\omega t}$, the tensor ε is therefore a complex quantity

$$\varepsilon_{ij} = \varepsilon'_{ij} + i\varepsilon''_{ij}. \tag{3.8}$$

If the absorption losses of the medium can be neglected, ε is a Hermitian matrix

$$\varepsilon_{ij} = \varepsilon^*_{ji}\,. \tag{3.9}$$

Furthermore, while in non-polarized medium ε_{ij} is symmetrical, in a magnetically saturated medium with magnetization $\mathbf{M}$, the generalized principle of symmetry for kinetic coefficients leads to the equivalence

$$\varepsilon_{ij}(\mathbf{M}) = \varepsilon_{ji}(-\mathbf{M})\,. \tag{3.10}$$

Following from eqs. (3.8), (3.9) and (3.10), one obtains

$$\begin{aligned} \varepsilon'_{ij}(\mathbf{M}) &= \varepsilon'_{ji}(\mathbf{M}) = \varepsilon'_{ij}(-\mathbf{M}) \\ \varepsilon''_{ij}(\mathbf{M}) &= -\varepsilon''_{ji}(\mathbf{M}) = -\varepsilon''_{ij}(-\mathbf{M})\,, \end{aligned} \tag{3.11}$$

therefore ε' is symmetrical and even function of $\mathbf{M}$, while ε'' is antisymmetrical and odd function of $\mathbf{M}$. The imaginary part ε'' can thus be represented in terms of a vector $\mathbf{G}$ using the antysymmetric Levi-Civita tensor, which will be symboled by e_{ijk} to avoid confusion with the permittivity

$$\varepsilon''_{ij} = e_{ijk} G_k\,. \tag{3.12}$$

Odd permutations of e_{ijk} lead to the definitions

$$\begin{aligned} -\varepsilon''_{zy} = \varepsilon''_{yz} &= G_x \\ -\varepsilon''_{xz} = \varepsilon''_{zx} &= G_y \\ -\varepsilon''_{xy} = \varepsilon''_{yx} &= G_z\,, \end{aligned} \tag{3.13}$$

and the displacement field can be expressed as

$$\begin{aligned} D_i = (\varepsilon'_{ij} + i\varepsilon''_{ij})E_j &= (\varepsilon'_{ij} + ie_{ijk}G_k E_j \\ \Rightarrow \mathbf{D} &= \varepsilon'\mathbf{E} + i(\mathbf{E}\times\mathbf{G})\,. \end{aligned} \tag{3.14}$$

Therefore, the displacement field $\mathbf{D}$ becomes function of the real symmetric matrix ε and of the vector $\mathbf{G}$, which is a real pseudovector called *gyration vector*. The direction of $\mathbf{G}$ is called the gyration axis of the material, and the material which satisfies the relations (3.14) is said to be *gyrotropic*. To first order $\mathbf{G}$ is proportional to the applied magnetic field

$$\mathbf{G} = \varepsilon_0 \chi^{(m)} \mathbf{H}\,. \tag{3.15}$$

In the previous equation, $\chi^{(m)}$ is the magneto-optical suceptibility tensor which appear in eq. (2.21). Eq. (2.21) is the fundamental expression for the description of the phenomenon under investigation in this work, and describes the non-linear responce of the magnetization to an oscillating electric field. In particular, the second-order dependence to the electric field in eq. (2.21) is determined by $\chi^{(m)}$. The permittivity can be expanded into power series of $\mathbf{M}$ since opto-magnetic effects are considerably small, and the gyration vector becomes

$$G_k = \sum_{\mu=1}^{3} f_{k\mu}\alpha_\mu + O(\alpha^3) \tag{3.16}$$

$$\varepsilon'_{ij} = (\varepsilon_0)_{ij} + \sum_{k,l=1}^{3} g_{ijkl}\alpha_k\alpha_l + O(\alpha^4) \tag{3.17}$$

$$g_{ijkl} = g_{jikl} = g_{ijlk} = g_{jilk} \tag{3.18}$$

where α_x, α_y and α_z, are the direction cosines of **M**, i. e. the cosines of the angles between **M** and the coordinate axes, and $f_{k\mu}$ and g_{ijkl} contain all the symmetry properties of the crystal, and are functions of the optical frequency w. The simplest case to analyze is when **G** is parallel to a principal axis, for example considering **M** along a [001] direction in a cubic crystal. One obtains, in cubic coordinate system, by keeping only the linear term α_z and using symmetry properties,

$$\varepsilon = \begin{bmatrix} \varepsilon_0 & if\alpha_z & 0 \\ -if\alpha_z & \varepsilon_0 & 0 \\ 0 & 0 & \varepsilon_0 + g\alpha_z^2 \end{bmatrix} = \begin{bmatrix} \varepsilon_1 & iG_z & 0 \\ -iG_z & \varepsilon_1 & 0 \\ 0 & 0 & \varepsilon_2 \end{bmatrix}. \tag{3.19}$$

It is evident that G_z is an eigenvector of ε with eigenvalue ε_2, while the other eigenvalues are identical. The off-diagonal terms give rise to the Faraday effect. In fact, the solutions for a wave propagating in the z direction, are elliptically polarized waves with phase velocities $1/\sqrt{\mu(\varepsilon_1 \pm G_z)}$, where μ is the magnetic permeability. The result is obtained from the expression $v = 1/\sqrt{\mu\varepsilon}$, by finding the eigenvalues of ε in the xy plane of the optical fields. The difference in phase velocities causes the Faraday effect.

In the case of magnetostatic spin-wave scattering with **M** parallel to z, one should consider also the linear terms α_x and α_y which may arise from higher order terms in eq. (3.18, 3). For a cubic crystal like YIG and using the cubic coordinate system, the $81 = 3^4$ components of g_{ijkl} can be reduced to 21 independent variables and one obtains

$$f_{k\mu} = f\delta_{k\mu},$$

$$g = \begin{bmatrix} g_{11} & g_{12} & g_{12} & 0 & 0 & 0 \\ g_{12} & g_{11} & g_{12} & 0 & 0 & 0 \\ g_{12} & g_{12} & g_{11} & 0 & 0 & 0 \\ 0 & 0 & 0 & g_{44} & 0 & 0 \\ 0 & 0 & 0 & 0 & g_{44} & 0 \\ 0 & 0 & 0 & 0 & 0 & g_{44} \end{bmatrix}. \tag{3.20}$$

In the expression above, $\delta_{k\mu}$ is the Kronecker delta function, and g is written in matrix form harnessing the Voigt notation [1] [39], [40]. In a cubic crystal the higher order terms which contain a first order term (as $\alpha_z^2\alpha_x$) do not exist. From eqs. (3.12), (3.18), the variation of the dielectric tensor can be written as

$$\begin{bmatrix} \delta\varepsilon'_{xx} \\ \delta\varepsilon'_{yy} \\ \delta\varepsilon'_{zz} \\ \delta\varepsilon'_{yz} \\ \delta\varepsilon'_{zx} \\ \delta\varepsilon'_{xy} \end{bmatrix} = \begin{bmatrix} g_{11} & g_{12} & g_{12} & 0 & 0 & 0 \\ g_{12} & g_{11} & g_{12} & 0 & 0 & 0 \\ g_{12} & g_{12} & g_{11} & 0 & 0 & 0 \\ 0 & 0 & 0 & g_{44} & 0 & 0 \\ 0 & 0 & 0 & 0 & g_{44} & 0 \\ 0 & 0 & 0 & 0 & 0 & g_{44} \end{bmatrix} = \begin{bmatrix} \alpha_x^2 \\ \alpha_y^2 \\ \alpha_z^2 \\ \alpha_y\alpha_z \\ \alpha_z\alpha_x \\ \alpha_x\alpha_y \end{bmatrix} \tag{3.21}$$

$$\begin{bmatrix} \delta\varepsilon''_{xx} \\ \delta\varepsilon''_{yy} \\ \delta\varepsilon''_{zz} \\ \delta\varepsilon''_{yz} \\ \delta\varepsilon''_{zx} \\ \delta\varepsilon''_{xy} \end{bmatrix} = \begin{bmatrix} 0 & 0 & 0 \\ 0 & 0 & 0 \\ 0 & 0 & 0 \\ f & 0 & 0 \\ 0 & f & 0 \\ 0 & 0 & f \end{bmatrix} = \begin{bmatrix} \alpha_x \\ \alpha_y \\ \alpha_z \end{bmatrix} \tag{3.22}$$

where $\delta\varepsilon'_{ij} = \delta\varepsilon'_{ji}$ and $\delta\varepsilon''_{ij} = -\delta\varepsilon''_{ji}$, from eq. (3.11). As previously mentioned about eq. (3.19), f is related to the Faraday effect.

[1] One identifies a symmetric pair ij of 3d indices with a multi-index I that has the range from 1 to 6:
$11 \to 1, 22 \to 2, 33 \to 3, 23 \to 4, 31 \to 5, 12 \to 6$

In our case, the $[110]$ direction of the sample is orthogonal to the magnetic field H_0, which defines the equilibrium position of **M**. Consequently, the problem is projected to a minor dimension, and the observed magnetization precession is described as a second-order process conveniently described by a third–rank tensor g_{ijk}.

CHAPTER 4

Characterization of the Hybridized System

In this chapter we characterize the hybridized system in the cavity-QED framework by means of microwave network analysis, in order to set the optimal experimental conditions for the investigation of the photoinduced opto-magnetic phenomenon. The characterization is performed in the frequency domain through measurements of the S-coefficients, which describe the behaviour of the system in terms of reflection and transmission of microwave signals. The transmission analysis allows to study the hybridezed modes and to examine the influence of the sample properties on the coupling regime, and the reflection coefficient allows to set the least perturbative detection condition at which the radiated power can be measured during the opto-magnetic excitation.

4.1 Experimental Setup

The experimental apparatus for the study of the hybridized system is pictorially shown in figure 4.1(a).

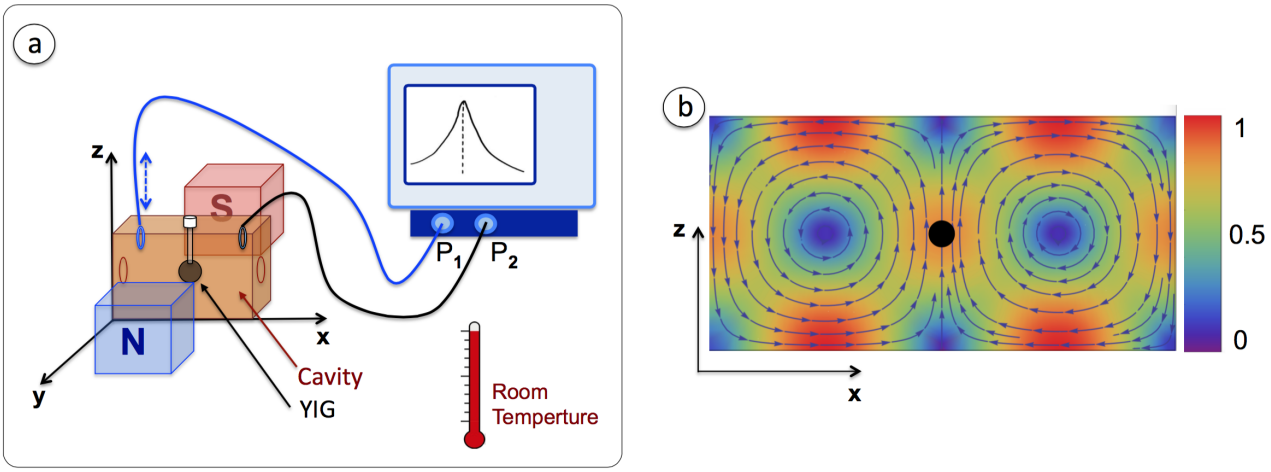

Figure 4.1: (**a**) Experimental set up. (**b**) Microwave magnetic field lines of the cavity TE_{102} mode.

We have analyzed the coupling regimes that take place in a microwave cavity with a 2 mm YIG sphere and of a 1.8 mm-diameter, 2.7 mm-length YIG cylinder. The sphere is glued to an alumina (aluminum–oxide) rod that identifies the crystal axis [110], while the cylinder is sustained by a support of the same material as illustrated in fig. 4.2.

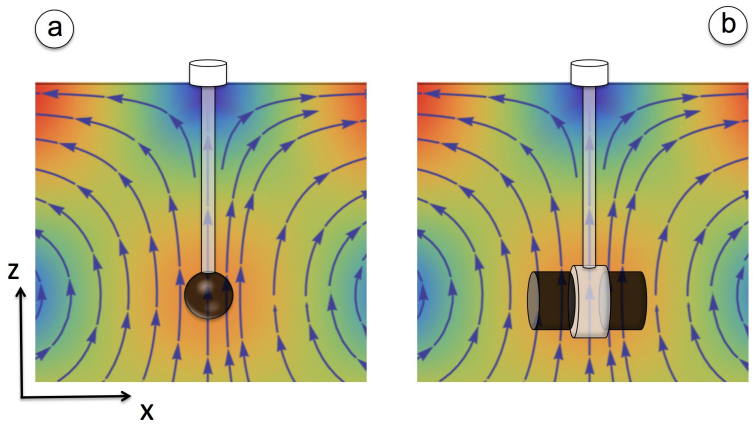

Figure 4.2: (**a**) Position of the spherical sample (Ferrisphere Inc) in the cavity TE_{102} mode. (**b**) Cylindrical sample (Deltronic) in the TE_{102} field lines.

The samples are set in the central point of a copper 3D rectangular microwave cavity with dimensions $98 \times 42.5 \times 12.6\,\text{mm}^3$, as shown in fig. 4.1. A static magnetic field H_0 is applied by means of an electromagnet in the y-direction orthogonal to the TE_{102} cavity mode. The spherical sample is therefore magnetized along its easy axis. The value H_0 can be varied by changing the electromagnet current. Figure 4.3 shows the typical values of magnetic field used in the measurements reported in this work.

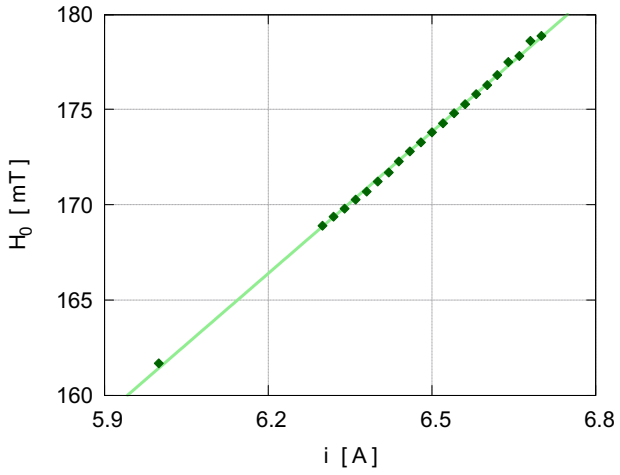

Figure 4.3: Linear dependence of H_0 to current supply.

Figure 4.1(b) shows the magnetic field profile of the TE_{102} mode, set by the boundary conditions $a_x = 98\,\text{mm}$ and $a_z = 42.5\,\text{mm}$:

$$B_x = \frac{A_x}{f_c a_z} \cos\left(\frac{\pi z}{a_z}\right) \sin\left(\frac{2\pi x}{a_x}\right) \tag{4.1}$$

$$B_z = \frac{A_z}{f_c a_x} \sin\left(\frac{\pi z}{a_z}\right) \cos\left(\frac{2\pi x}{a_x}\right) \tag{4.2}$$

where c is the light velocity, $A_{x,z}$ are normalization constants and $f_c = c/2\sqrt{(1/a_z)^2 + (2/a_x)^2} \approx 4.67\,\text{GHz}$ is the TE_{102} mode frequency. The cavity has been designed in such a way that the frequency of its TE_{102} mode is within the stability range of the laser oscillator ($4.6 \div 4.7\,\text{GHz}$), in order to allow the tuning of the laser repetition rate to the resonance frequency of the hybridized system.

The cavity is equipped with an adjustable position antenna and a fixed one, that allow the characterization of the TE_{102} mode, of the hybridized modes, and detection of the radiated field in the cavity.

4.2 Characterization in the frequency domain

A two-port network is realized when the two antennae are connected to the ports P_1 and P_2 of a S-parameter Network Analyzer (mod. Agilent 8720ES). We then analyze our system with the scattering matrix or S-matrix formalism [54].

4.2.1 S-parameters

Scattering parameters or S-parameters are the elements of a scattering matrix or S-matrix that describes the electrical behavior of linear electrical networks when undergoing various steady state stimuli by electrical signals. For a two-port network, the ports being numbered $i = 1, 2$, the associated S-parameter definition is in terms of incident and reflected power, namely a_i and b_i (fig. 4.4). For each port the reflected power may be defined in terms of the S-parameter matrix and the incident power waves by the equation

$$\begin{pmatrix} b_1 \\ b_2 \end{pmatrix} = \begin{pmatrix} S_{11} & S_{12} \\ S_{11} & S_{12} \end{pmatrix} \begin{pmatrix} a_1 \\ a_2 \end{pmatrix} \tag{4.3}$$

However if, according to the definition of S-parameters, port 2 is terminated in a load identical to the system impedance Z then, by the maximum power transfer theorem, b_2 will be totally absorbed making a_2 equal to zero. Therefore, defining a_1 and a_2 as the incident voltage waves and b_1 and b_2 as the reflected waves, one obtains $S_{11} = b_1/a_1$ and $S_{12} = b_1/a_2$, and in general $S_{mn} = S_{nm}$. Hence, the two-port S-parameters have the following generic descriptions:

- S_{11} is the input port voltage reflection coefficient
- S_{12} is the forward voltage gain
- S_{21} is the reverse voltage gain
- S_{22} is the output port voltage reflection coefficient.

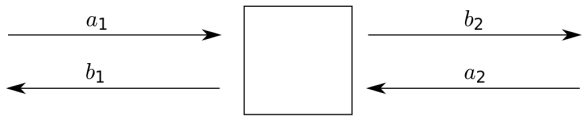

Figure 4.4: Two-port network diagram.

The S-parameters are functions of the system impedence and of the system frequency.

4.2.2 S_{11}-coefficient

In the measurements realized in this thesis, as explained in sec. 2.1.3, the cavity framework allows to measure the power radiated during the opto-magnetic excitation. This is not the case in the free field measurements, where the coupling between the antenna and the YIG sample emission is unknown. In order to do so it is necessary to set the apparatus in critical coupling condition, which corresponds to the minimum of the reflection coefficient at one cavity port. In this case the radiated power is twice the power dissipated on the transmission line, adapted tp 50Ω at resonance and in critical coupling

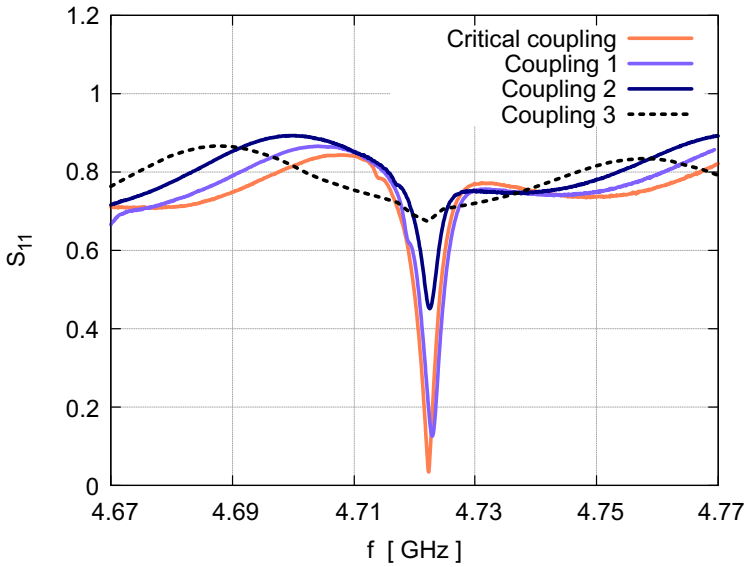

Figure 4.5: Measurements of the S_{11}-parameter for different coupling strength of the input coupler, corresponding to different z-positions of the antenna. The y-axis units are 'milliunits', which refer to the ratio of the reflected to the incident power.

[54]. Figure 4.5 shows measurments of S_{11} of the mobile cavity antenna for different couplings to the cavity mode.
The orange data represent the optimal working condition, where the S_{11} coefficient reaches the minimum value (underlined by the dashed line in figure).

4.2.3 S_{12}-coefficient

The S_{12} coefficient allows to study the cavity modes (frequency and linewidth) and to systematically investigate the hybridized modes for different values of the applied external field. Figure 4.6(a) displays a map of the S_{12} coefficient as function of H_0 (B_{ext} in figure). The measurement is performed with a spherical YIG sample.
The colour map is a collection of 400 spectra of S_{12} registered for different values of H_0. One can clearly distinguish an avoided resonance crossing (ARC) at the center of the figure, which is the signature of a regime of strong coupling, as reminded by fig. 4.6(b) reported in sec. 2.4.1. As the Larmor frequency $f_L = \gamma_e H_0/2\pi$ is tuned to the cavity mode f_c, the hybridized mode frequency f_- e f_+ reach a minimum separation. This is the previously discussed ARC, when f_L coincides with f_c.

Figure 4.7 (a) displays the S_{12} coefficient registered at $H_0 = 0$ (red data), which coincides with the empty cavity spectrum, and the S_{12} at the ARC point ($H_0 \approx 171\,\mathrm{mT}$). Figures 4.7 (b), (c) remind the theoretical behaviour of strongly coupled oscillators in terms of energy cycles and total dissipated power, as derived in sec. 2.4.1.
When the material is not magnetized, the experimental data have been fitted with a Lorentian function in the form:

$$S_{12,cav}(f) = A\frac{1}{2\pi}\frac{\Gamma}{(f-f_c)+\left(\frac{\Gamma}{2}\right)^2}, \tag{4.4}$$

where A is a normalization parameter, Γ and f_c are respectively the FWHM and mean value of the Lorentian function. The fit function for the hybrid system is the real part of the transmission function of the standard input-output formalism [53, 55, 47, 48, 49, 4],

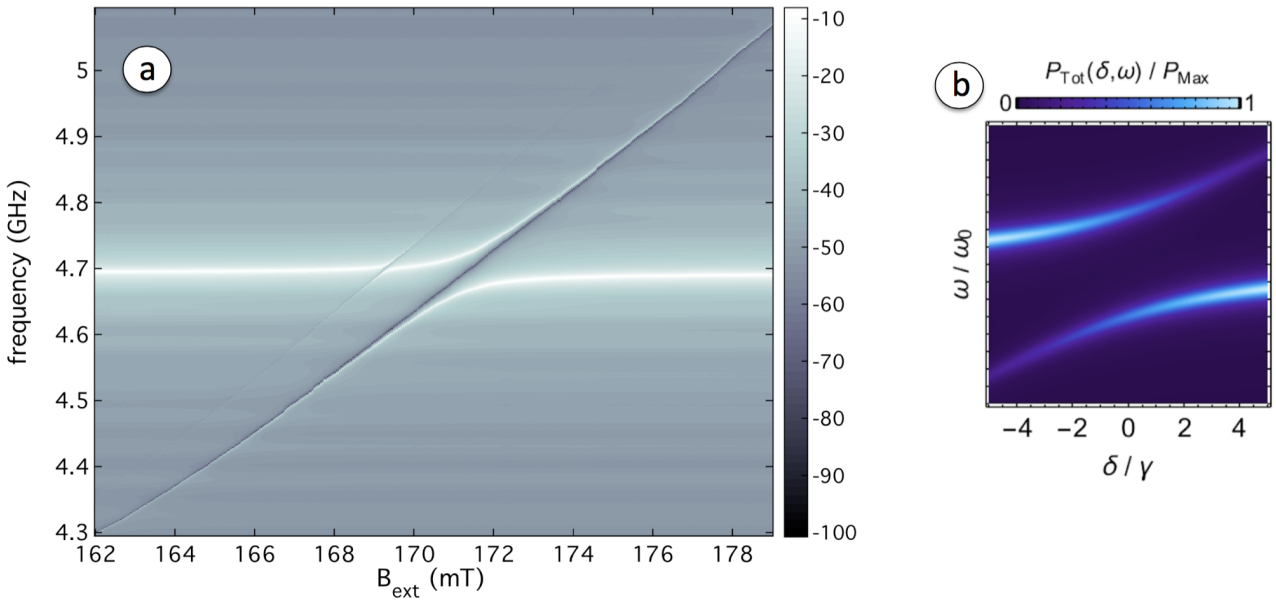

Figure 4.6: (**a**) Map of S_{12} coefficient as functions of H_0 (B_{ext} in figure). The measurment is performed with a spherical YIG sample. (**b**) Reminder of the theoretical simulation for the total normalized dissipated power of two strongly coupled harmonic oscillators, as reported in sec. 2.4.1.

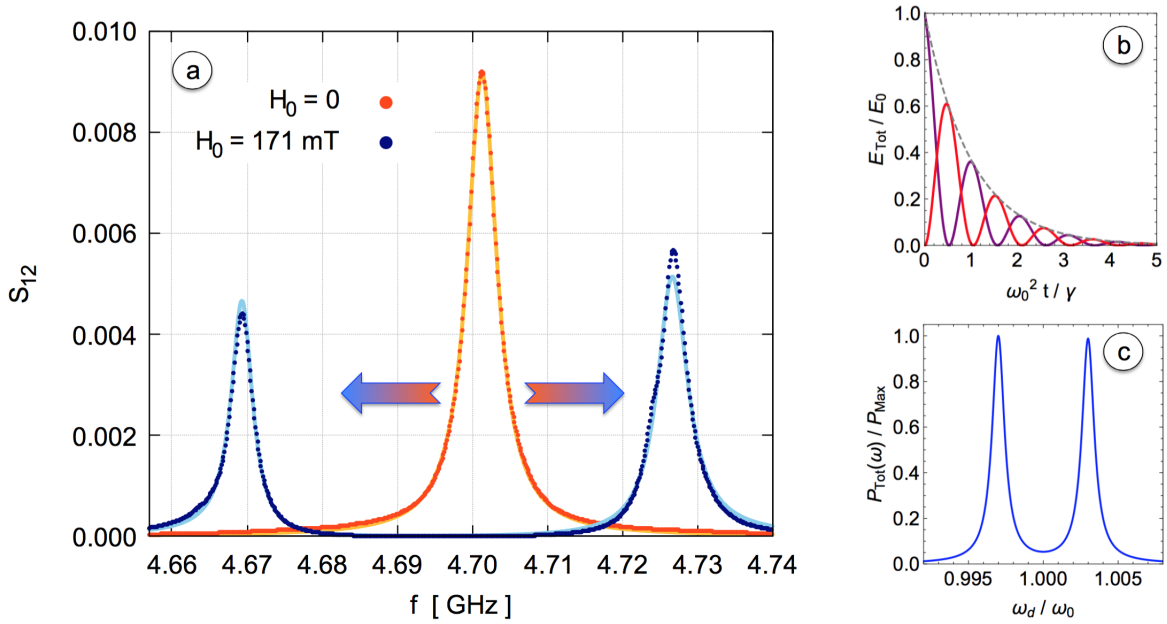

Figure 4.7: (**a**) S_{12} spectra of the cavity (red data) and the hybrid system YIG-cavity (blue data) in the frequency domain, for a spherical YIG sample. The cavity resonance is fitted with a Lorentian distribution, while the hybrid resonance is fitted with eq. 4.5. (**b**) Reminder of the simulation of energy cycles of a pair of strongly coupled harmonic oscillators, as reported in sec. 2.4.1. (**c**) Reminder of the simulation of the total normalized dissipated power of strongly coupled harmonic oscillators, as reported in sec. 2.4.1.

$$\mathbb{R}(S_{12,hybr}(\omega)) = \mathbb{R}\left(\frac{\sqrt{k_1 k_2}}{i(\omega-\omega_c) - \frac{k_1+k_2+k_{int}}{2} + \frac{|g_m|^2}{i(\omega-\omega_{FMR})-\gamma_m/2}}\right), \tag{4.5}$$

where ω_{FMR} and γ_m are the frequency and linewidth of the FMR mode, ω_c and $k_c/2\pi = (k_1 + k_2 +$

$k_{int})/2\pi$ are the frequency and total linewidth of the cavity and g_m is the coupling strength of the FMR mode to the cavity mode. The fit parameters of eqs. 4.4, 4.5 are

Q_0	Γ [MHz]	f_c [GHz]
955 ± 2	4.923 ± 0.010	4.701 ± 0.001

Table 4.1: Fit parameters of $S_{12,cav}$, related to the red data in fig. 4.7(a).

f_{FMR} [GHz]	f_c [GHz]	γ_m [MHz]	g_m/π [MHz]	$k_c/2\pi$ [MHz]
4.692 ± 0.003	4.704 ± 0.002	13.7 ± 0.2	56.1 ± 0.4	6.1 ± 0.1

Table 4.2: Fit parameters of $S_{12,hybr}$, related to the red data in fig. 4.7(a).

As first remark, the values for f_c are compatible within 2σ, therefore eq. 4.5 provides an indirect measurement of the cavity resonance. The frequency separation between the hybridized modes $f_- = 4.6694\,\text{GHz}$ and $f_+ = 4.7265\,\text{GHz}$ gives the coupling strength g_m/π (compatible within 3σ).
The coupling strength g_m allows to estimate a fundamental quantity of our physical system, i.e. the total number of electron spin N_s involved in the magnetic precession. In fact, g_m is equal to $g_0\sqrt{N_s}$ [50], [51], where $g_0 = \frac{\gamma_e}{2\pi}\sqrt{\mu_0 h f_c/V_c}$ is the coupling strength of a single spin to the cavity mode, with V_c the cavity volume, γ_e the gyromagnetic ratio of the electron, μ_0 the permeability of vacuum and h the Planck constant. From the fit parameters in table 4.2 we find $N_s = (5.4 \pm 0.1) \times 10^{19}$.
The decay time for the hybridized modes, can be calculated as $\bar{\tau} \equiv \tau_\pm = (2/\tau_c + 2/\tau_2)^{-1}$, where $\tau_c = 2/k_c$ and τ_2 are the loaded cavity decay time and the spin–spin relaxation time, respectively. One obtains $\bar{\tau} \approx 60\,\text{ns}$, compatibly with the expected value given by the manufacturer.

4.2.4 Influence of Sample Properties on Coupling

In the considered hybridized system, the cavity mode profile is fixed as determined by the designed geometry. The coupling regime of the hybridized system is thus mainly influenced by the sample properties and its orientation in the cavity [4].
In fig. 4.6 (a), the YIG sample was carefully oriented in such a way that only the uniform magnetization mode coupled to the selected cavity mode. As explained in sec. 3.0.5, second order magnetostatic modes can also be excited, as shown in fig. 4.6 (a) where one can distinguish a second much smaller anti-crossing at $\approx 169\,\text{mT}$.

Second Order Magnetostatic Modes

In second order magnetostatic modes the phases of the electron spin precessions might be different in different parts of the sphere, causing more than one resonant frequency for a given value of H_0 [37], which stand out in the transmission spectrum as 'notches'. Such modes can arise due to various mechanisms. In fact, provided that one has properly oriented the crystal in the cavity, and that the static magnetic field H_0 and microwave field amplitude are uniform in the sample volume, nevertheless spurious frequencies may come from the interaction with close metallic surfaces, for an image charge effect. In fact, it can be shown [38] that the coupling to higher order magnetostatic modes depends on the quantity D/λ, where D and λ are the diameter of the spherical sample and the wavelength corresponding to the frequency in question. Being the coupling weaker for smaller D, an advantageous condition to avoid spourious resonant modes is working with small specimens ($1 \div 2\,\text{mm}$ is a proper dimension for $\approx$GHz microwave resonators).

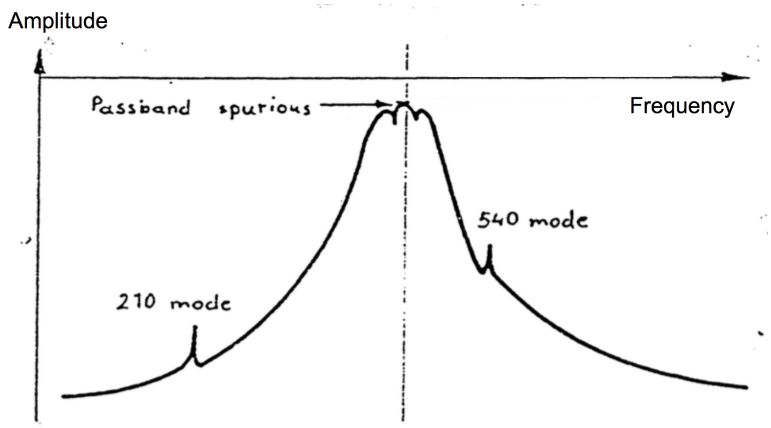

Figure 4.8: Transmission microwave spectrum of a YIG film. Higher order magnetic modes are visible in form of notches.

A typical transmission spectrum with notches due to higher order magnetic modes is shown in fig. 4.8 [56] for a YIG film.
Figure 4.9 displays the arise of a notch in a transmission measurement for the YIG-cavity system.

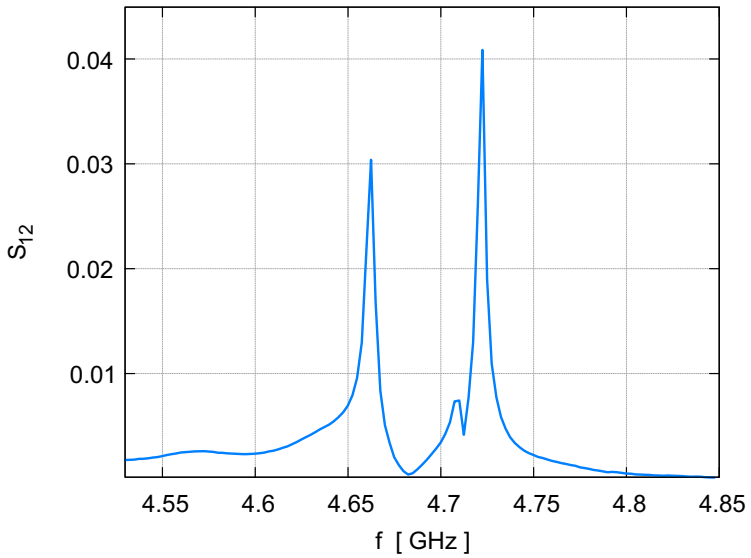

Figure 4.9: S_{12} spectrum of the hybridized system in the frequency domain, with the spherical YIG sample. A second order mode of magnetization arises as a notch.

Sample Geometry

We have also investigated the influence of the sample shape on the coupling regime of the hybrid system. We had three different available YIG samples, two spheres of the same dimensions, one intact and one slightly laser-damaged, and a cylinder. Figure 4.10 displays the S_{12} spectrum for the three different cases.
Figure 4.10 (a) shows the S_{12} spectra for the spherical YIG samples, in which the *blue data* refer to the intact sphere and the *black* data stand for the damaged sphere. Even though the damage was limited to a very small portion of the sphere surface, a factor 2 linewidth increase is observed, as reported in table 4.3 through the fit parameters of eq. 4.5.

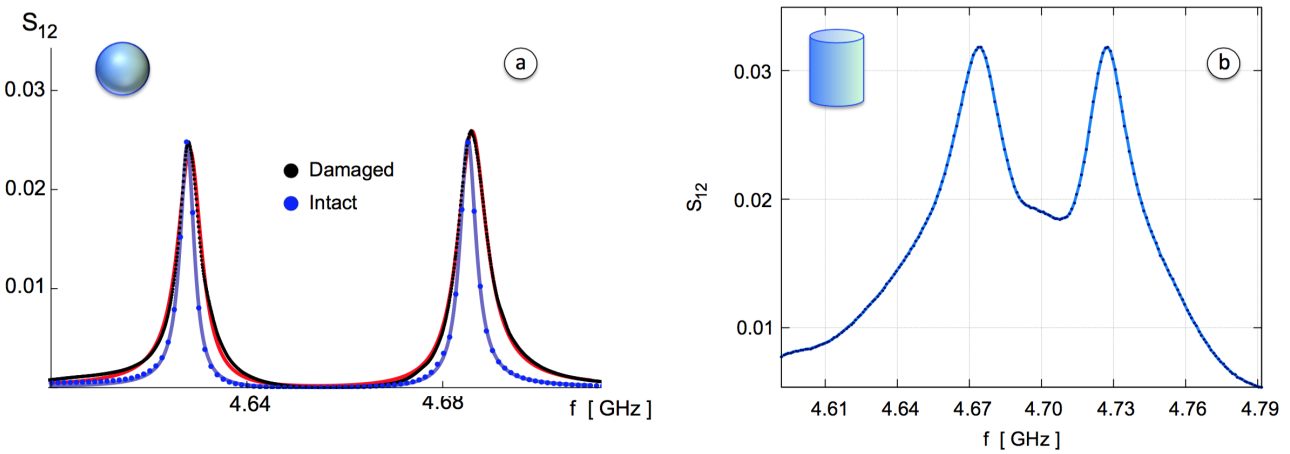

Figure 4.10: (**a**) S_{12} spectrum of the hybridized system in the frequency domain, with the spherical YIG sample. The *blue* data represents the transmission signal for an intact sphere, while the *black data* represents the transmission signal for a damaged sphere. In particular, the blue data are normalized to the black data, to make the comparison of linewidths clearer. The data are fitted with eq. 4.5. The damaged sample exhibit larger linewidths. (**b**) S_{12} spectrum of the hybridized system in the frequency domain, for cylindrical YIG sample. The experimental data are linked by a graphic line, for clarity.

	f_{FMR} [GHz]	f_c [GHz]	$g_m/2\pi$ [MHz]	γ_m [MHz]	$k_c/2\pi$ [MHz]
Intact	4.694 ± 0.001	4.699 ± 0.001	57.1 ± 0.2	1.5 ± 0.1	7.77 ± 0.02
Damaged	4.694 ± 0.001	4.700 ± 0.002	57.2 ± 0.4	3.0 ± 0.2	12.76 ± 0.03

Table 4.3: Fit parameters for P_{hybr} in fig. 4.10(a).

Figure 4.10 (b) shows the S_{12} spectrum for the cylindrical YIG sample. The linewidths are in this case comparable with the frequency difference between the hybridized modes (≈ 60 MHz), and therefore the coupling regime is weak, as explained in sec. 2.4.1. The remarkable linewidth increase is caused both by the cylinder orientation in the cavity and by its geometrical structure. Its orientation in the resonator is determined by the necessity of aligning the laser beam propagation axis with the sample longitudinal axis so to avoid lens effects, in the optical scheme for the photoinduced excitation. The cylinder longitudinal axis also coincides with its easy magnetization axis, since it was fabricated for being a Faraday rotator, but in our set up the electromagnet structure is such that the only possible direction of H_0 is orthogonal to it, i.e. along y, as shown in fig. 4.1 (a). Therefore, with this orientation of the sample, the geometrical conditions for inducing uniform magnetostatic modes in a cylinder (see sec. 3.0.5) are not respected, i.e. the static magnetic field H_0 is not parallel to the easy magnetization axis of the sample, nor to its longitudinal axis x, and also the TE_{102} mode lines are orthogonal to x, with consequent shape effects which produce non-uniformities of the magnetic fields and the arise of second order magnetic modes.

CHAPTER 5

Photoinduced magnetization precession

The systematic study of the phenomenon in this thesis has been possible only thanks to a special laser system that was previously developed [57, 59, 58, 60]. In such a laser, pulses are delivered not only at high peak power to access the non-linear regime in materials, but also at high repetition rates, i.e. at several GHz, at the Larmor precession frequency in ferrimagnets.

5.1 The laser system

The laser system used to optically drive the magnetization is pictorially shown in figure 5.1 (a), (b), and in the picture in fig. 5.13 (c). It is a high-energy solid-state laser in a master-oscillator power-amplifier (MOPA) configuration, seeded by a 5 GHz repetition-rate, mode-locked oscillator. The output pulses are delivered in bunches of ≈ 2000 pulses (macro-pulse), and their energy can be as high as $\approx 100\,\mu$J at the 1064 nm-wavelength.

As we want to work in the YIG transparency window ($1.5 \div 5\,\mu$m, see fig. 5.2) to avoid thermal effects, we make use of optical non-linear elements to convert the 1064 nm-wavelength output to different wavelengths. Second harmonic generation (SHG) is used to pump an optical parametric oscillator (OPO) and generate ≈ 800 nm (signal) and ≈ 1550 nm (idler) beams. In the present measurements we use both the 1064 nm and the 1550 nm-wavelength outputs at maximum pulse energy of few μJ.

The laser design is described in detail in refs. [57, 59, 58, 60], and the relevant characteristics are summarized in the caption of fig. 5.1.

Figure 5.4 shows the laser oscillator comb spectrum with its fundamental harmonic at $f_R \approx 5$ GHz, and its successive harmonics $n_i \times f_R$, i=1, 2, 3. The spectrum was registered at a 20 GHz sampling oscilloscope with an ultrafast photodiode set after the amplification stage (PD1 in fig. 5.1 (a)). In the new method that we use to optically drive the magnetization, we tune the f_R to the Larmor precession frequency of the ferrimagnet, but in principle each harmonic of the spectrum can be used to drive the optical excitation, as explained in sec. 2.2.2.

The microwave field emitted during the magnetization precession is detected by an antenna critically coupled to the cavity TE_{102} mode, and observed after amplification at a 6 GHz sampling oscilloscope. Figure 5.5 shows the gain curve (blue) of the amplifier, with the red curve being a zoom in the linear amplification range, which gives a 39 dB-gain, compatible with the values specified by the manifacturer.

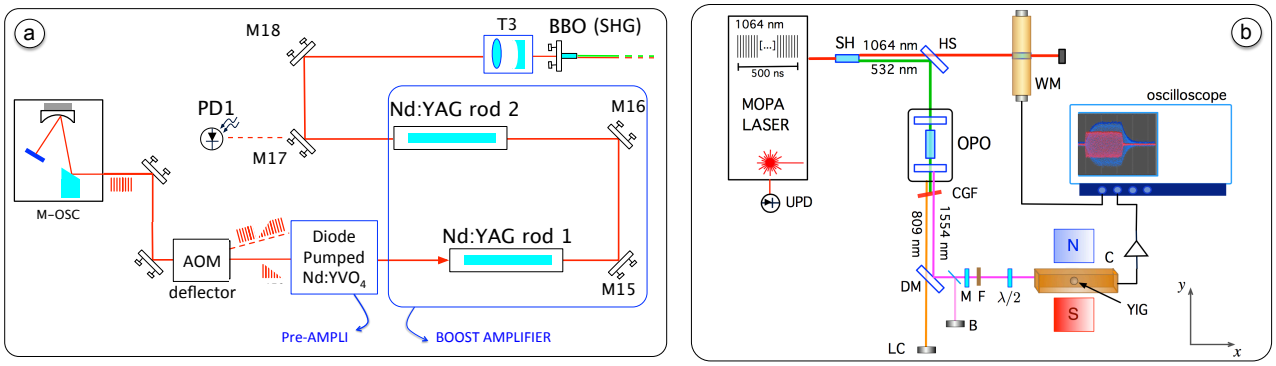

Figure 5.1: Conceptual setup of the laser system. (**a**) [60] The master oscillator (M-OSC) is a V-folded diode-pumped cavity with Nd:YVO_4 active medium, which provides a cw-train at 1064 nm at $f_R \approx 5$ GHz repetition rate. An acousto-optic modulator (AOM) selects a train of picosecond pulses (macro-pulse), repeated at $f_T = 1$ Hz, whose number and exact envelope profile can be controlled to compensate for amplification distortions by acting on the radio-frequency signal driving the acousto-optic device. A diode-based pre-amplification stage and a lamp-pumped amplification stage allow to achieve up to $\approx 100\,\mu$J 12 ps-duration pulses. (**b**) [61] The 1064 nm macro-pulse is frequency–doubled (SH) to pump an optical parametric oscillator (OPO). The 809 nm OPO output is monitored at a laser camera (LC) through a 1000 nm–cutoff dichroic mirror DM, while the 1550 nm OPO output is directed on the YIG sphere through several optical filters (CFG, F, M). The laser repetition rate, macropulse uniformity and energy are monitored at an InGaAs ultrafast photodiode (UPD), a coaxial waveguide device WM [**?**], and bolometer B respectively. HS is an harmonic separator (HR at $\lambda = 532$ nm, HT at 1064 nm). The microwave field emitted during the magnetization precession is detected by an antenna critically coupled to the cavity TE_{102} mode, and observed at a 6 GHz sampling oscilloscope, via a 39 dB–gain amplification stage.

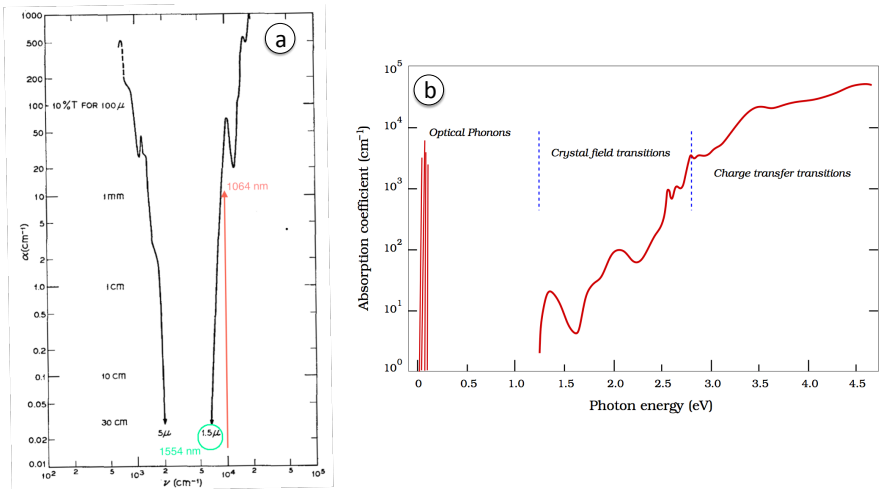

Figure 5.2: Optical absorption of YIG, in the frequency (**a**) and energy (**b**) domain.

5.1.1 Optical non-linear stage

In order to obtain good generation efficiency and beam profile quality of the 1550 nm OPO output, the second-harmonic generation (SHG) and OPO cavity were carefully adjusted before every measurement.

SHG is a second order nonlinear process of frequency mixing with the initial waves (pump and signal) having a common frequency, i.e. $f_p = f_s = f = c/1064\,\text{nm}$, and the idler wave having $f_i = 2f = c/532\,\text{nm}$, with c light velocity. OPO generation is also a second order nonlinear process, which

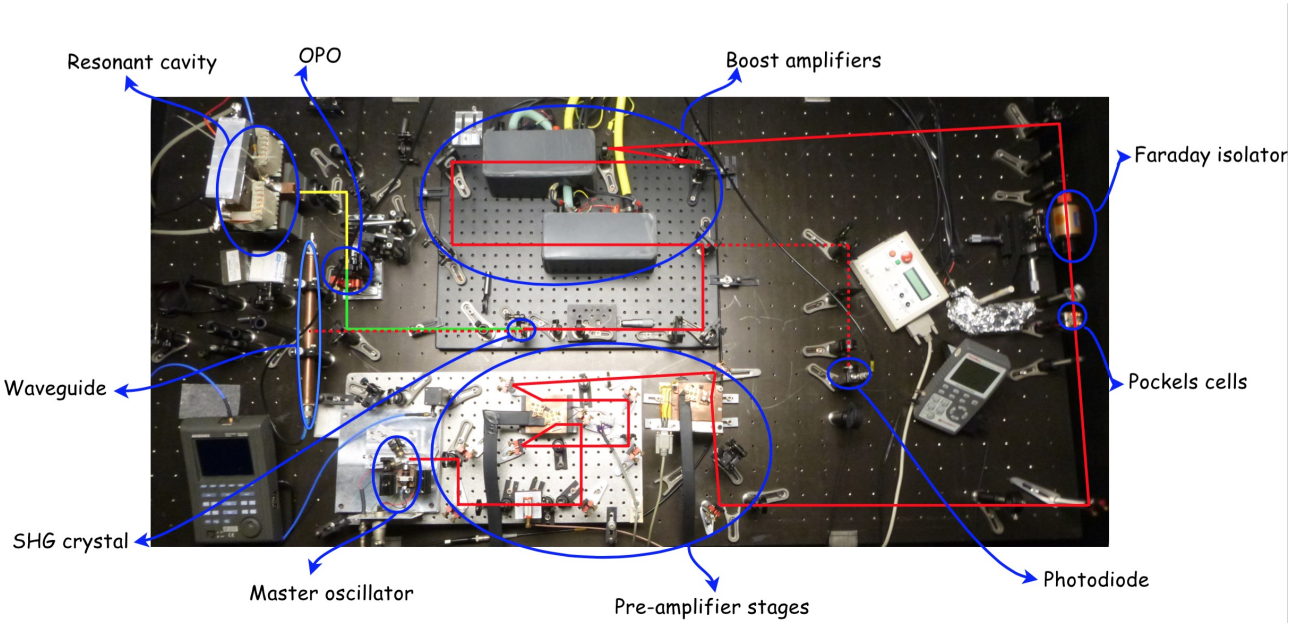

Figure 5.3: Picture of the laser optical table.

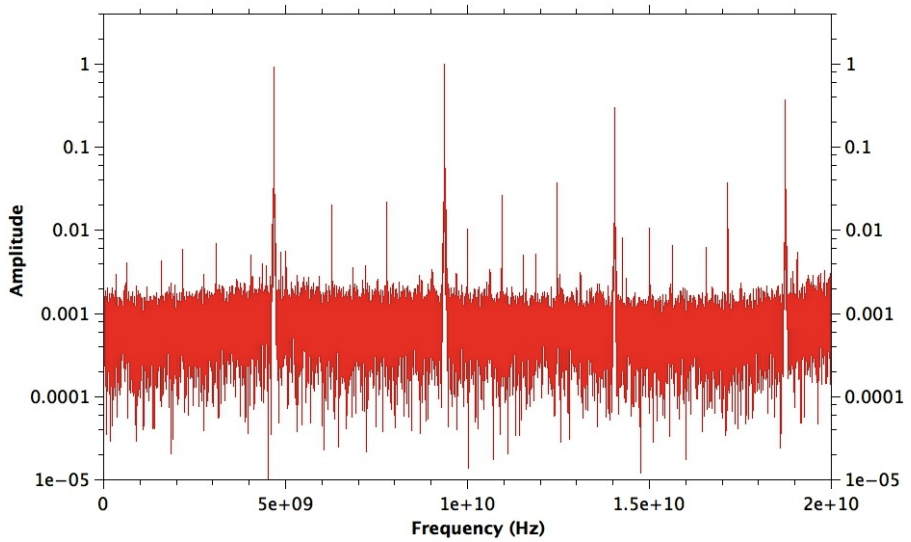

Figure 5.4: Laser oscillator comb spectrum, with its fundamental harmonic at $f_R \approx 5\,\text{GHz}$, and its successive harmonics $n_i \times f_R$, i=1, 2, 3. The spectrum was registered at a 20 GHz sampling oscilloscope with an ultrafast photodiode set after the amplification stage (PD1 in fig. 5.1 (a)).

drives the conversion of the incident beam frequency into two different output frequencies, i.e. $1/\lambda_p = 1/\lambda_s + 1/\lambda_i$, where in our case $\lambda_p = 532\,\text{nm}$, $\lambda_s \approx 808\,\text{nm}$ and $\lambda_i \approx 1550\,\text{nm}$.
Laser beam alignment, polarization control, regulation of beam dimensions, and adjustement of the SH non-linear crystal position allowed to obtain $\approx 40\%$ efficiency of 532 nm-wavelength conversion. The SHG output beam was then used to synchronously pump an optical parametric oscillator (OPO) plane-plane cavity, designed to obtain a singly-resonant oscillator operating around 800 nm. After beam alignement, and adjustement of the cavity mirrors and non-linear crystal orientation, in our experiment we managed to obtain the 1550 nm output with $\approx 10\%$ generation efficiency with a pump energy of 20 mJ. To enhance the quality in the output beam profiles fine regulation of the OPO cavity mirrors was performed, through maximization of the 809 nm output power at the bolometer (B in fig. 5.1 (b)), and by observing the 809 nm output spacial profile through fluorescence of a white paper

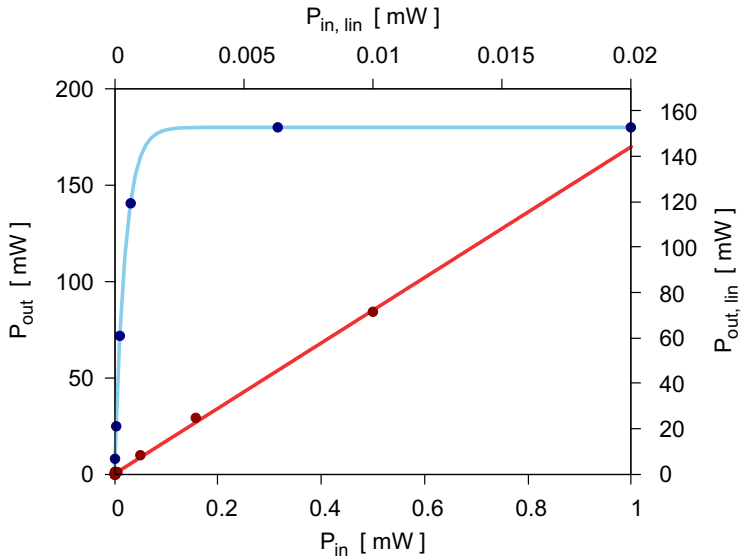

Figure 5.5: Amplification curve (blue data), and detail of the linear amplification range (red curve).

screen set at more than 2 m distance of the oscillator.

5.1.2 Beam profiles

The measurement of the beam dimensions was performed by means of a Coherent laser camera for the 1064 nm-wavelength beam, and by means of the knife-edge tecnique for the near infra-red 1550 nm OPO output. In figure 5.6 the colour map and gaussian profiles of the 1064 nm-wavelength beam (a) and knife-edge measurements of the 1550 nm-wavelength beam (b) are shown, with the beam waists reported in tables. The knife-edge fit function is reminded below:

$$f(x) = A \cdot \mathrm{erfc}\left(\frac{x - x_0}{w_x}\right), \tag{5.1}$$

with A normalization constant, w_x beam waist, and x_0 the mean value of the intensity gaussian distribution along the x-direction.
While the 1064 nm-wavelength beam ehibits circular profile (fig. 5.6(a)), the 1550 nm-wavelength beam is elliptical, as reported in the table in fig. 5.6(b), and with the longer axis in the OPO phase-matching plane [**?**]. The turquoise fit functions refer indeed to different axes of the beam section (the black data are measured along the x-axis, the red data along the y-axis) measured in the same experimental conditions. Beside phase-matching effects, the OPO output profile is also very sensitive to the alignement of the oscillator components. As an example, the light-blue fit function shows an x-axis knife-edge measured at different experimental conditions, which exhibits indeed a different waist.

5.2 Detection in the free field scheme

The scheme that was initially designed for the observation of the optically driven spin precession is very simple, and it involves a single loop-antenna coupled to the YIG sample that undergoes the action of multi-GHz laser pulses in free field. This has been experimentally implemented as shown in fig. 5.7 (a). A crossed loops scheme, displayed in fig. 5.7 (b) allows for measurements of the FMR linewidth through the S-coefficients, as shown in the experimental data of fig. 5.8 (a), (b). Note that the loops are set at 90° to each other in order to have $S_{12} \approx 0$ when the YIG sphere is not present.

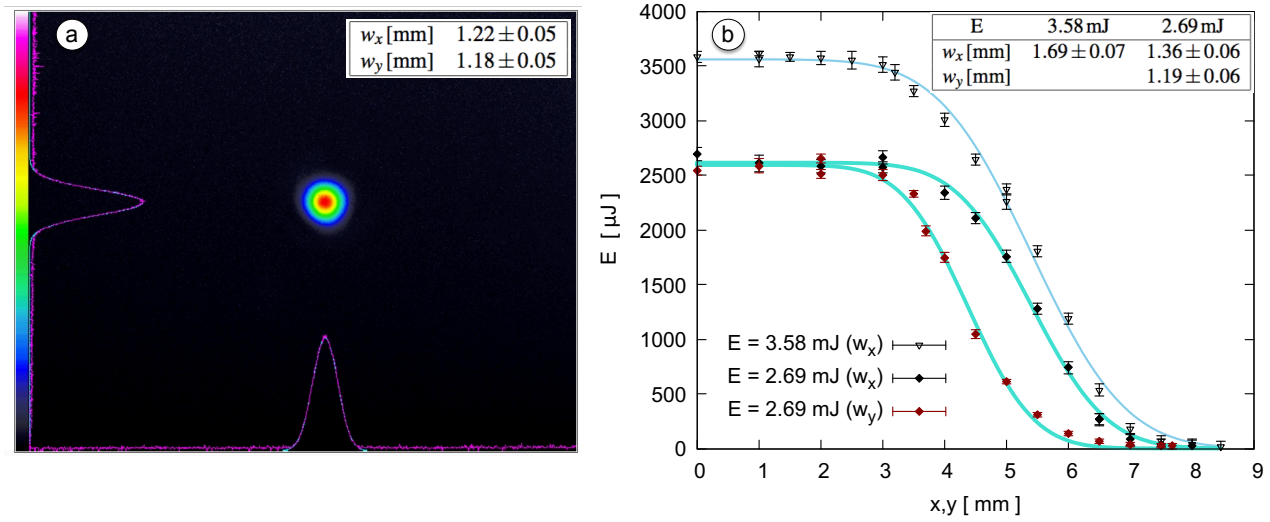

Figure 5.6: (**a**) Beam colour map of 1064 nm-wavelength beam measured with a Thorlabs laser cam. Beam waists are shown in figure. (**b**) Knife-edge measurements of 1550 nm-wavelength beam. The black data refer to knife-edge profiles along the y-axis (parallel to optical table), while the red data refer to a knife-edge profile along the z-axis (orthogonal to optical table). The measurments along the x-axis were repeated for different values of the macro-pulse energy. Beam waists are shown in figure.

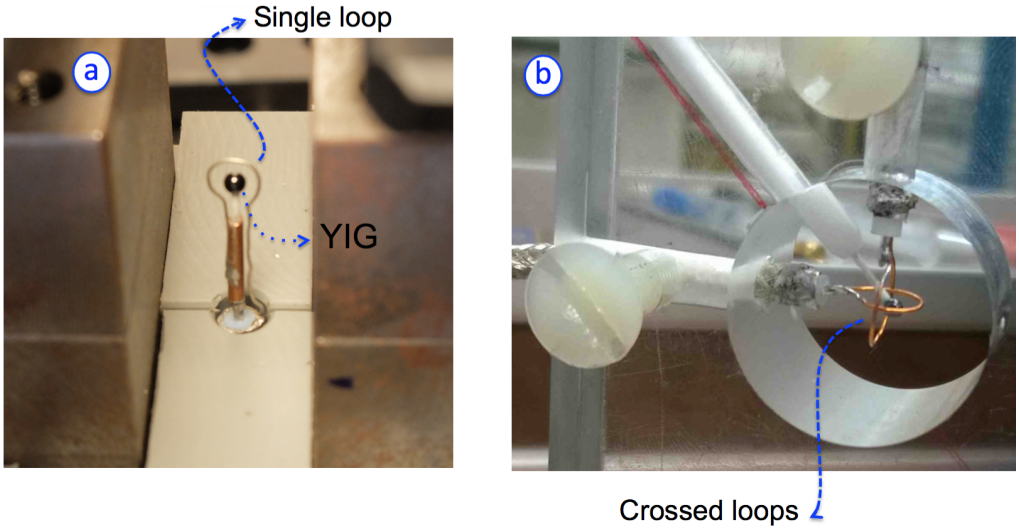

Figure 5.7: Pictures of the free field scheme. (**b**) Detail of the single loop scheme. (**c**) Detail of the crossed loops scheme.

5.2.1 S-coefficients

Similarly to the procedure described for the cavity-QED framework in chap. 4, the magnetic behaviour of the YIG sample in free field is characterized by means of S_{11} and S_{12} coefficients, shown in figure 5.8. The minimum of the reflection coefficient in fig. 5.8 (a) corresponds to the Larmor frequency f_L. By regulating the value of the magnetic static field H_0, the FMR frequency f_L is set within the stability range of the laser oscillator $\approx [4.6 \div 4.7]$GHz. Then the laser repetition rate f_R is tuned to f_L and the apparatus described in subsec. 5.1 is used to investigate the opto–magnetic phenomenon.
Incidentally, by varying H_0 and recording the corresponding Larmor frequency through S_{11}, a measurement of the gyromagnetic ratio of the electron $\gamma_{e,exp}$ is obtained, as shown in fig.5.9. The an-

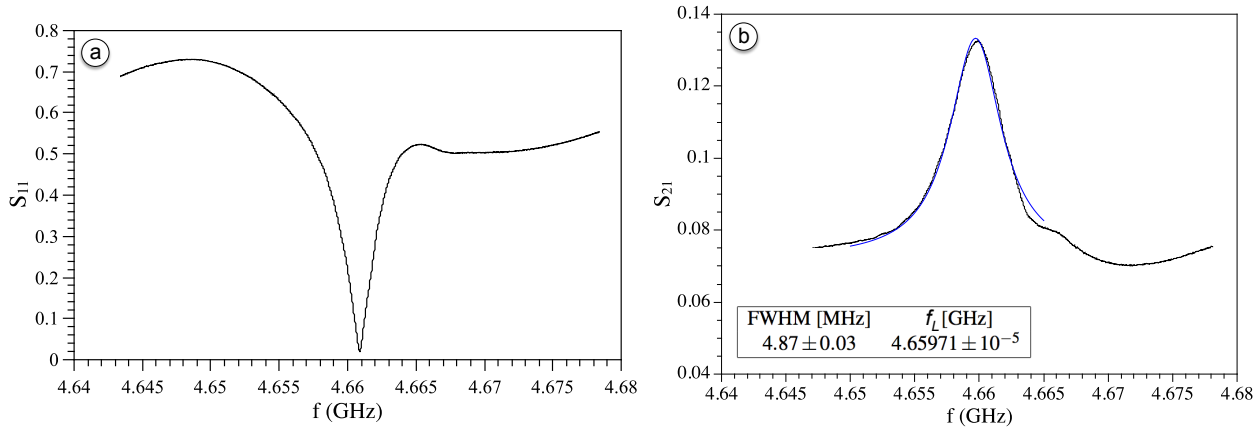

Figure 5.8: Two-ports network analysis performed with the two crossed loop-antennae scheme. (**a**) S_{11} coefficient in linear scale. (**b**) S_{12} coefficient in linear scale. A Lorentian function fit it shown, with the fit parameters reported in the table.

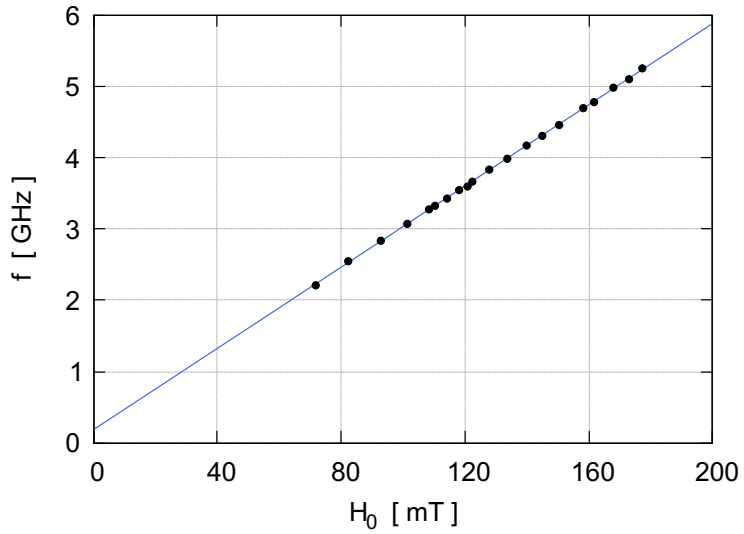

Figure 5.9: Linear dependence of the Larmor frequency from the static magnetic field.

gular coefficient of the linear fit corresponds $\gamma_{e,exp}$, which is compatible with the nominal value $\gamma_e = 28.0\,\text{GHz/T}$. Remarkably, the linear offset is not compatible with the origin, which might be an evidence of the presence of internal fields in the material which add up to H_0.

5.2.2 Photoinduced magnetization precession

In this section we demonstrate that the photinduced magnetization precession is a FMR phenomenon, and that the linewidth we measure under optical excitation coincides with the linewidth measured through the S_{12} coefficient. This purpose is accomplished in two ways:

- at fixed H_0, by varying the laser repetition frequency f_R and registering the maximum amplitude of the microwave emitted signal in the cavity (at stationary condition in the time domain);
- at fixed f_R, by varying H_0 and registering the corresponding maxima amplitudes of the signal.

Microwave radiated signal

When the laser pulses repetition frequency f_R is tuned to the Larmor frequency f_L, and the macro-pulse impinges on the YIG sample surface, the emitted microwave radiation signal is registered at the oscilloscope, and it is displayed in fig. 5.10 (a). In figure 5.10 (a) the 500 ns-duration laser macro-pulse envelope (blue data) is also shown.

Figure 5.10(b) shows the envelope of the microwave signal at $f_R \approx 4.661$ GHz. The signal does not istantaneously reach the maximum amplitude, but its growth is described by a characteristic time τ given by the exponential fit $f(t) = a(1 - e^{-\frac{t-t_0}{\tau}})$, with a normalization constant, in the time range from $t_0 = 0$ to 500 ns. Similarly, the signal decay is fitted to $f(t) = be^{-\frac{t-t_0}{\tau}}$. At resonance (fig. 5.10 (c)), the characteristic times coincide (≈ 70 ns), as expected when a cavity is excited by a pulsed microwave generator (see appendix A). When the laser repetition frequency is detuned from the Larmor

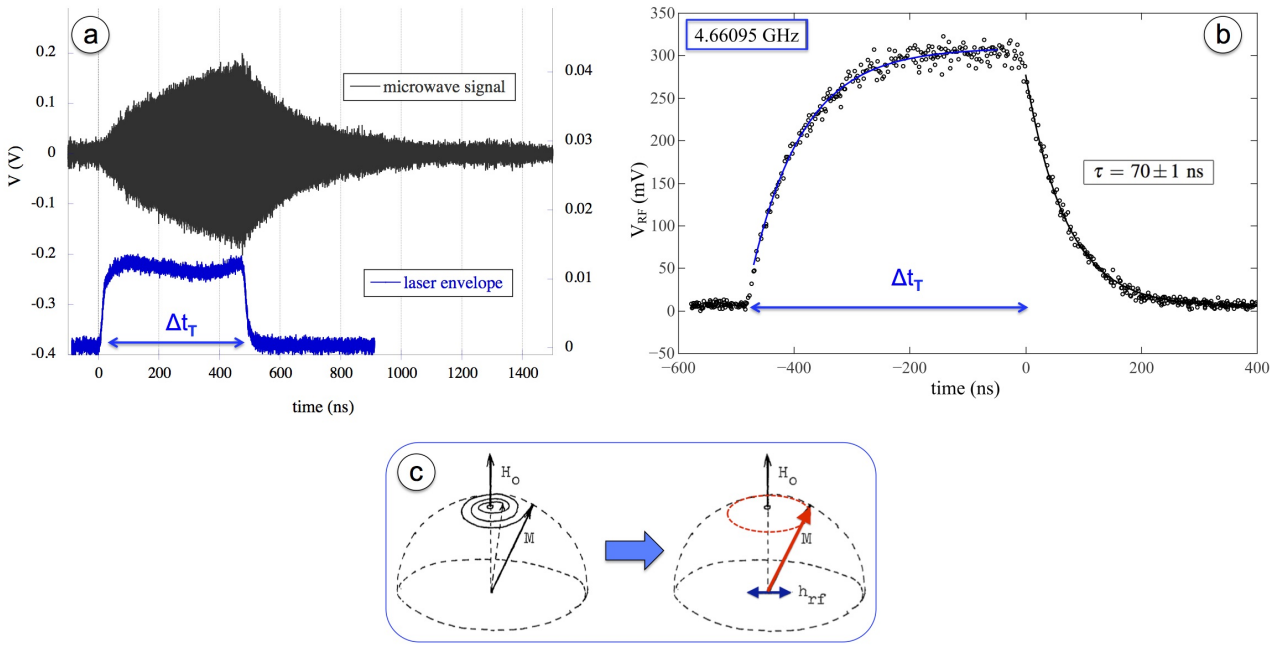

Figure 5.10: (**a**) Emitted signal (black data) and laser macro-pulse envelope (blue data), when f_R is close to the Larmor frequency. The laser envelope is registered at an ultrafast photodiode, as explained in sec. 5.1. (**b**) Envelope of the microwave signal detected with the loop coupled to the YIG sphere, at resonance. (**c**) Pictorial representation of the optically driven magnetization precession at $f_R = f_L$.

frequency of $\delta f = f_R - f_L$, the microwave signal is considerably different from the one shown in fig. 5.10 (a), (b).

Figure 5.11 (a) shows the signal obtained at $\delta f = 10.3$ MHz. Due to detuning, the excitation process suffers of dissipation with a consequent decrease in the growth time and a maximum profile amplitude reduced to $\approx 1/3$ compared to fig. 5.10 (b). The beats amplitude decays exponentially until equilibrium is reached after a transient time of ≈ 300 ns, when the magnetization is forced to precede at the laser repetition frequency. Fitting the signal with a sinusoidal function with exponential decay, one obtains the beat frequency, that is compared in table 5.1 with the nominal frequency difference between the laser repetition rate and the measured Larmor frequency.

In general, the fit parameters are qualitatively comparable with the expected value $\delta f = f_R - f_L$, but half of the values are not compatible within the errors. The analysis does not consider in fact systematic errors such as electromagnet hysteresis effects, not perfect compensation of the laser macro-pulse envelope, slight perturbations of the sample position...

f_R [GHz]	δf [MHz]	f_{beat} [MHz]
4.6465	15.3	14.3 ± 0.4
4.6485	13.3	13.0 ± 0.3
4.6515	10.3	9.3 ± 0.3
4.6539	7.9	7.1 ± 0.2
4.6673	5.5	6.0 ± 0.6
4.6693	7.5	7.8 ± 0.3
4.6742	12.4	13.3 ± 0.6

Table 5.1: Fit parameters (fig. 5.11(a)).

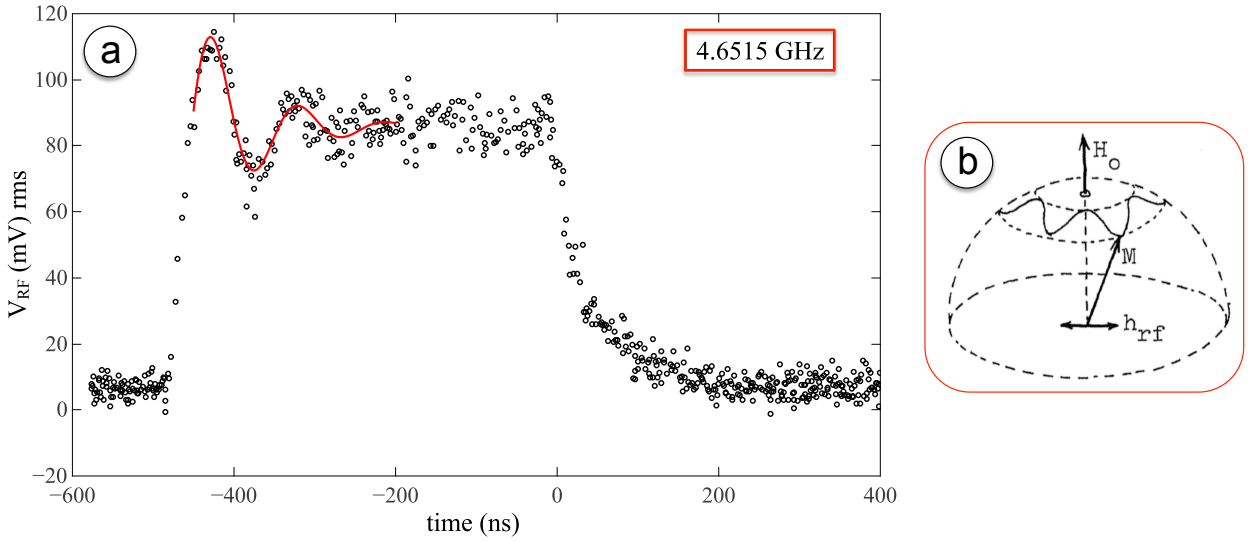

Figure 5.11: (**a**) Envelope of the emitted microwave signal at $\delta f = 10.3\,\text{MHz}$ and $f_R = 4.6515\,\text{GHz}$. The beat is fitted to a sinusoidal function of frequency δf with exponential decay. (**b**) Pictorial representation of the magnetization precession at $\delta f \neq 0$, after the driving force is 'switched off'.

FMR resonance

Figure 5.12 displays the FMR curves measured according to the previously mentioned dual methods, with $V_{RF}(H_0)$ maximum amplitude of the microwave signal at fixed H_0 ($f_L = 4.6618\,\text{GHz}$), and $V_{RF}(f_R)$ maximum amplitude of the microwave signal at fixed repetition rate of the laser pulses $f_R = 4.6609\,\text{GHz}$.
The resulting FMR resonance curves are fitted to Lorentian functions, and the fit parameters are reported in table 5.2.

function	f_0 [GHz]	FWHM [MHz]
$V_{RF}(H_0)$	4.6595 ± 0.0001	7.8 ± 0.4
$V_{RF}(f_R)$	4.6601 ± 0.0002	7.3 ± 0.6

Table 5.2: Fit parameters (fig. 5.12).

The FWHMs are compatible within the errors, while the mean values are slightly different. This is due to the systematic errors also previously mentioned, in fact the $V_{RF}(f_R)$ data obtained by changing H_0 suffer from hysteresis effects which are not present in the other data.
The FMHFs measured with the dual method are compatible within the errors. They are instead not

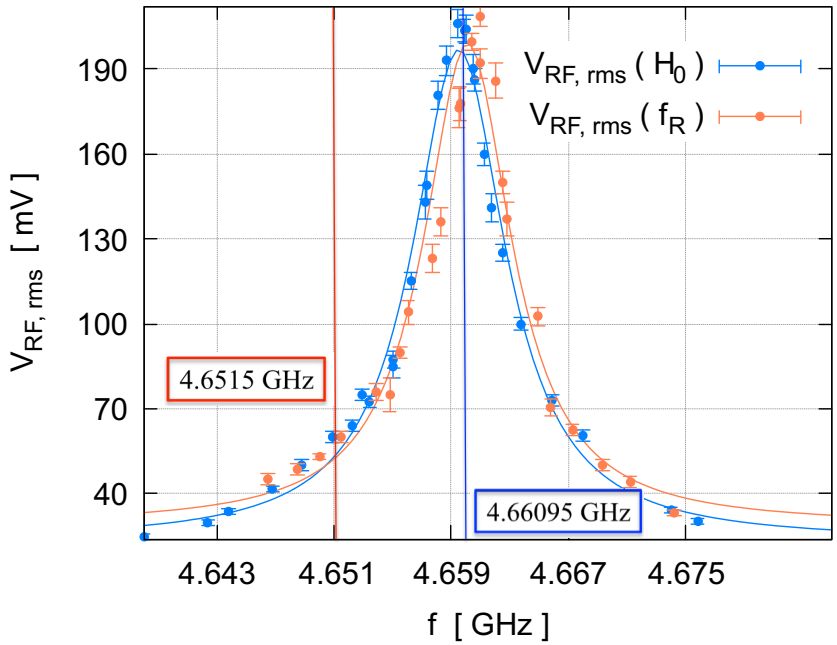

Figure 5.12: Amplitudes of the emitted microwave signal at stationary regime of excitation, as functions of the detuned frequency. The voltage values are measured as root mean square (rms) within the plateau region (at steady-state) of the emission profile, with the associated rms error. The blue data are measured at fixed H_0 and by varying f_R, the coral data at fixed f_R and varying H_0. The vertical lines n the figure mark the f_R values associated to the signals shown in fig. 5.11 (a) (red line) and in fig. 5.10 (b).

compatible with the value obtained by analysis of the S_{12} coefficient in fig. 5.8 (b), due to the finite duration of the optical excitation. In fact, harmonics of the macro-pulse, that last 500 ns, have 2 MHz linewidth. We do not expect the mean values to be compatible as the hysteresis was not considered.

5.3 Detection in the cavity scheme

When the YIG samples are enclosed inside the microwave cavity, as described in chapter [**?**], the cavity resonance splits in two lines and we tune the laser repetition frequency f_R to the smaller frequency hybridized mode f_-. Laser light is allowed to enter the cavity through two small (3,mm-diameter) apertures on the smallest area opposite cavity walls, as shown in fig. 5.13, and detection is accomplished by means of a transmission line (see fig. 5.13 (a)) connected to the critically coupled loop.

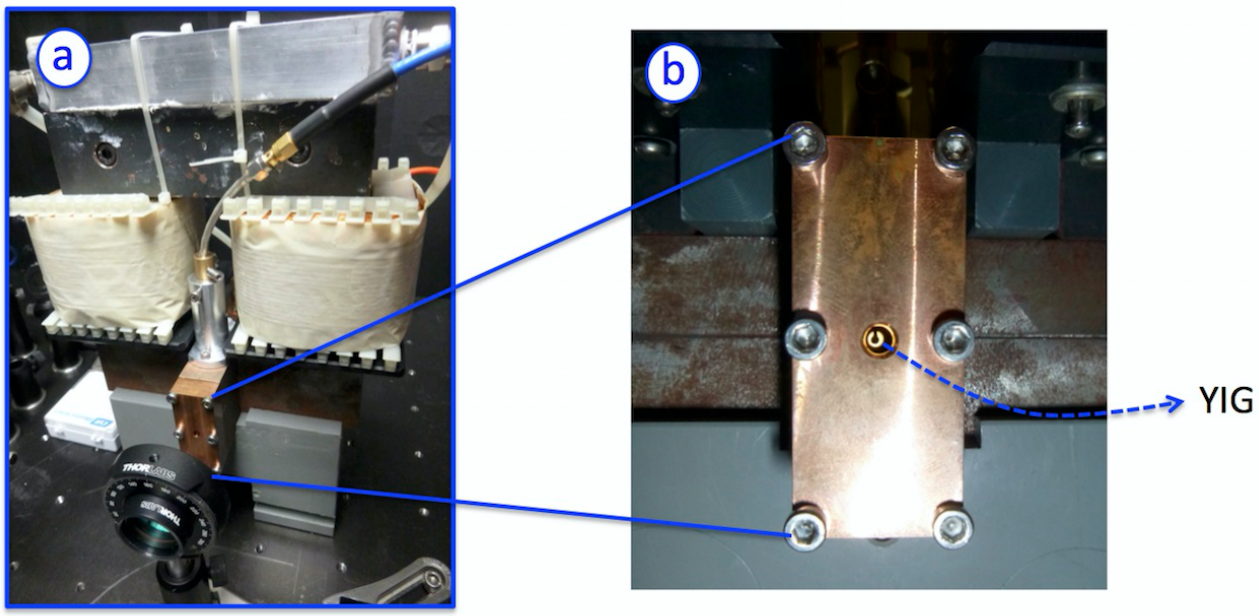

Figure 5.13: (**a**) The microwave cavity between the poles of the electromagnet. (**a**) Detail of the cavity, apertures and YIG sphere sample.

5.3.1 Microwave signal coherence

In order to verify whether the microwave signal generated in the cavity is in phase with the laser pulses, the device WM shown in fig. 5.1 (b) is used. Its working principle is described in ref. **??**). Figure 5.14 displays both the microwave signal detected in the cavity (blue data) and the laser macropulse monitor output (coral data) at resonance. It is worth noticing that the duration of the laser excitation is greater than the characteristic time of the system $\bar{\tau} \approx 60\,\text{ns}$, therefore we succeed to drive the magnetization precession in a steady-state regime. The characteristic time τ obtained by fitting the rise τ_{gr} and decay τ_{gr} of the signal and the steady-state voltage $V_{Hy,st}$ are reported in table 5.3. They are optimally compatible as expected at resonance, and they are moreover compatible with the expression of the relaxation time $\bar{\tau} \equiv \tau_{\pm} = (2/\tau_c + 2/\tau_2)^{-1}$ derived through the S_{12} analysis of sec. 4.2.3.

τ_{gr} [ns]	τ_{dec} [ns]	$V_{Hy,st}$ [mV]
57 ± 2	59 ± 1	70.4 ± 0.1

Table 5.3: Fit parameters (fig. 5.14).

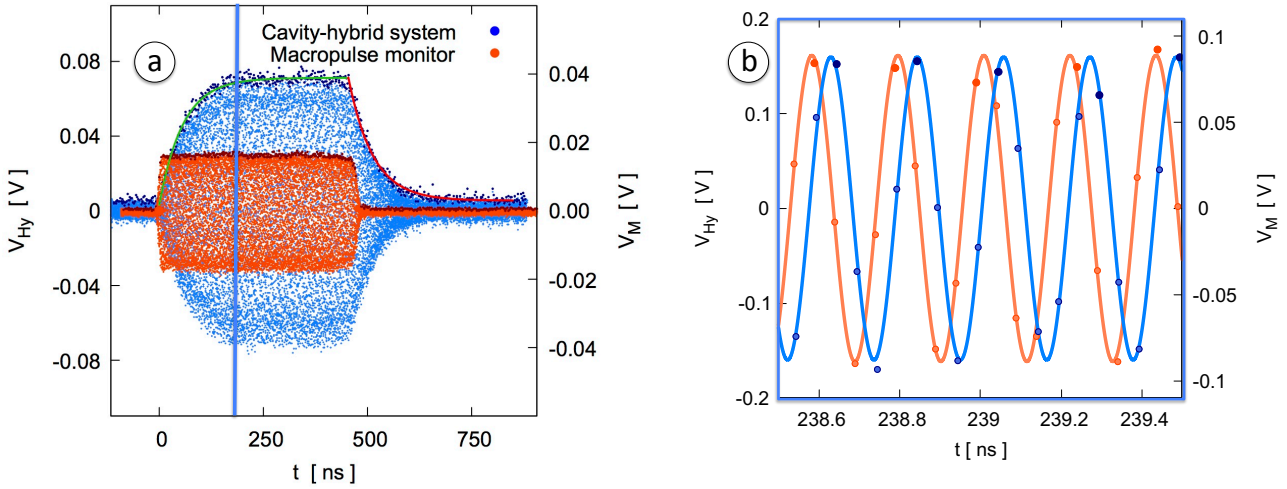

Figure 5.14: (**a**) Microwave signal generated in the cavity (blue data) and laser macro-pulse monitor (coral data), at resonance ($f_R = f_- = 4.6729\,\text{GHz}$). **b** Juxtaposition of the signals in a nanosecond time range, with sinusoidal fittings to the experimental data.

The juxtaposition of the microwave signal detected in the cavity and of the laser macro-pulse monitor signal in fig. 5.14 (b) demonstrates that we manage to drive the magnetization precession in phase with the laser pulses.

We note that if the laser repetition rate is not tuned to the hybridized mode frequency f_-, the signal maximum value is smaller than $V_{Hy,st}$ measured at resonance. Moreover beats are observed as in the free field configuration. The greater is the detuning $\delta f = f_R - f_-$ the more dissipative is the system dynamics, as shown in the microwave signal envelopes of figure 5.15 (a) and pictorially illustrated in fig. 5.15 (b).

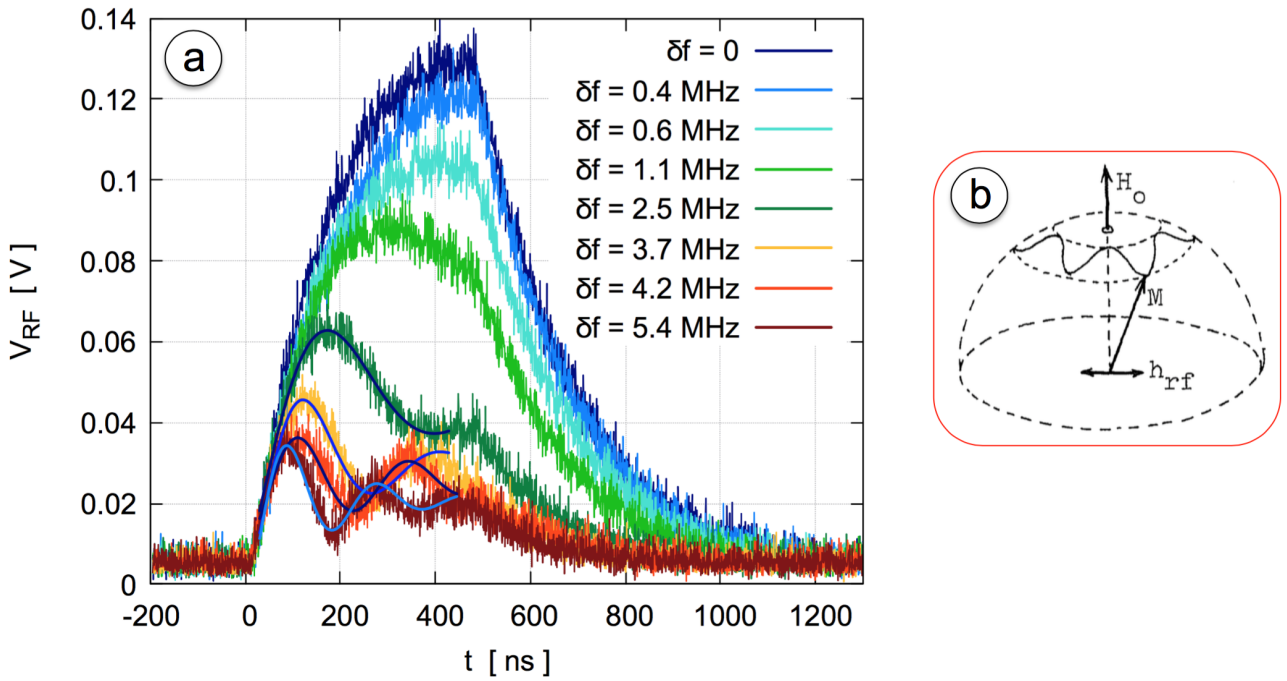

Figure 5.15: (**a**) Microwave signal envelopes for different values of detuning $\delta f = f_R - f_-$. The beats are fitted to sinusoidal functions with exponential decay. (**b**) Pictorial illustration of the beating effects arising in the magnetization dynamics when $\delta f \neq 0$.

As also observed in the free field configuration, beats in the signal profiles have exponential decay, which indicates that after a transient time the magnetic system response is suppressed and it is forced to precede at $f_R \neq f_-$, with the maximum signal amplitude strongly reduced by dissipation. By using sinusoidal functions with exponential dacay, we compare the nominal frequency difference δf between the laser repetition frequency and the measured Larmor frequency (through S coefficients), with the experimental fit parameter for the beating frequency, as reported in table 5.4.

f_R [GHz]	δf [MHz]	f_{beat} [MHz]
4.6607	2.5	2.2 ± 0.1
4.6595	3.7	3.5 ± 0.2
4.6590	4.2	4.3 ± 0.2
4.6578	5.4	5.3 ± 0.2

Table 5.4: Fit parameters (fig. 5.15).

5.3.2 FMR resonance

We investigate the resonant behaviour of the phenomenon around the hybridized mode frequency f_- by varying the laser repetition rate f_R and measuring the correspondent maximum amplitude of the microwave radiated signal, as shown in figure 5.16. The maximum amplitude is in this case reported in the plot as maximum of the discrete Fourier transform (DFT) of the data, in order to perform deconvolution of the microwave signal measured in the cavity from the optical signal , by division of their DFTs (convolution theorem). In the figure, the deconvoluted (blue) data are compared to the measured convoluted data (red).

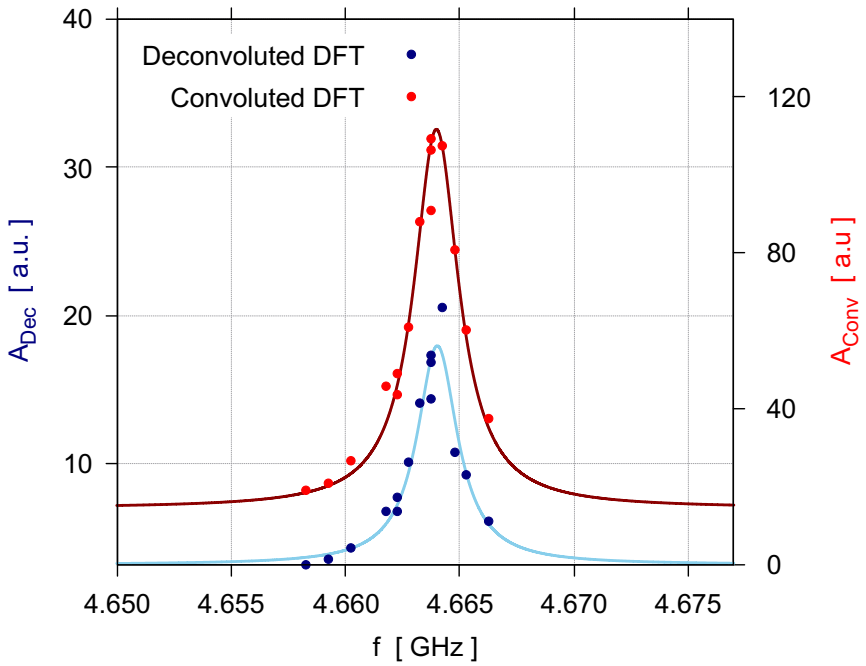

Figure 5.16: Amplitude of the discrete Fourier transform (DFT) of the microwave radiated signal (red data), at fixed $f_- = 4.664\,\text{GHz}$ and by varying the laser repetition rate f_R. The blue data are deconvoluted from the optical signal (convolution theorem).

We indeed demonstrate an optically induced FMR phenomenon also for the hybridized system, and

we fit the data to Lorentzian curves whose FWHMs are reported in table 5.5. The linewidths are $\approx 1/3$ of the values reported in table 5.2 for the free field.

FWHM_{conv} [MHz]	FWHM_{deconv} [MHz]
2.4 ± 0.1	2.1 ± 0.1

Table 5.5: Fit parameters (fig. 5.16.)

5.3.3 Hybridized modes

A further analysis tool is obtained by Fourier transform (DFT) of the signal registered in the time domain at the oscilloscope. In fig. 5.17 (a) we show the DFT of the microwave signal corresponding to the hybridized system with spherical YIG sample under 2.4 MW/cm^2 pulses intensity.

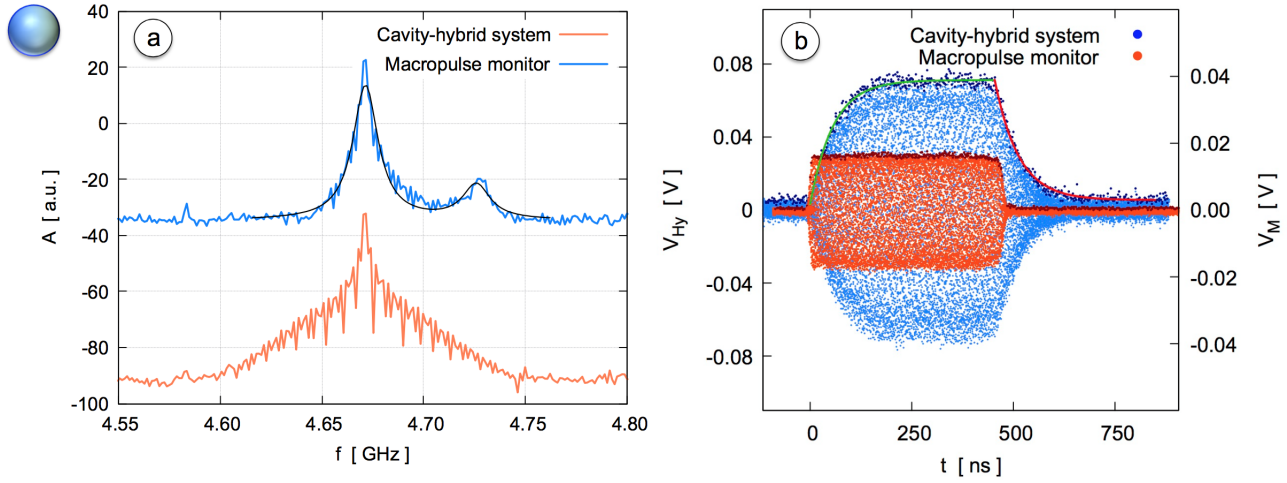

Figure 5.17: (**a**) DFTs of the microwave radiated signal of the hybridized system with spherical YIG, up-shifted of 40 dB (blue data), and of the laser macro-pulse monitor (coral data). The laser intensity was set to 2.4 MW/cm^2 and the measured beam waists in the horizontal and vertical direction were $d_x = 1.4$ mm and $d_y = 1.2$ mm. The data are fitted to a double Lorentian curve (black). (**b**) Reminder of fig. 5.14 (a).

It is noteworthy that the spectral component f_+ of the hybridized system is also excited, but with a much smaller strength, even if the laser repetition frequency f_R is tuned to f_-. This suggests that the coupling regime between the hybridized modes opens a channel of energy exchange from the excited to the non-excited eigenfrequency of the system. The experimental data are fitted to a double Lorentian function (black line), and the fit parameters are reported in table 5.6, together with the relaxation times of fig. 5.17 (b). From the experimental parameters we can derive a frequency separation of

f_- [GHz]	f_+ [GHz]	FWHM_- [MHz]	FWHM_- [MHz]	τ_{gr}	τ_{dec}
4.6714 ± 0.0002	4.726 ± 0.001	15.1 ± 0.7	16 ± 3	57 ± 2	59 ± 1

Table 5.6: Fit parameters (fig. 5.17).

the hybridized modes $\Delta f = f_+ - f_- = (55 \pm 1)$ MHz, which is compatible with the coupling strength $g_m/\pi = 57$ MHz measured through the S_{12} microwave analysis in sec. 4.2.3. These results shows that

each laser macro-pulse acts as an effective microwave field on the ensemble of strongly correlated spins, and therefore that we manage to optically excite the uniform FMR magnetostatic mode of the system.

Figure 5.18 displays the same analysis performed on the cylindrical YIG sample.

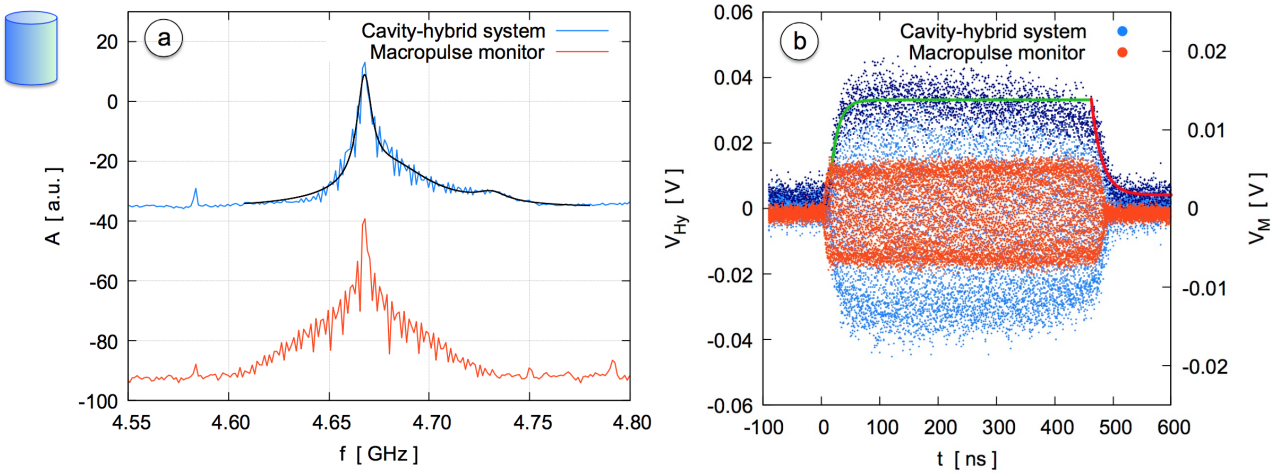

Figure 5.18: (**a**) DFTs of the microwave radiated signal of the hybridized system with cylindrical YIG, up-shifted of 40 dB (blue data), and of the laser macro-pulse monitor (coral data). The blue data are fitted to a triple Lorentian curve. (**b**) Microwave radiated signal (blue data) and laser macro-pulse monitor (coral data) in the time domain. The microwave signal profile is highlighted with darker colour and exponential fits are shown for the signal growth and decay.

In this case, the blue data in figure 5.18 (a) exhibit an only barely excited f_+ hybridized mode, with the additional presence of a second-order magnetostatic mode which distorts the spectrum, which is qualitatively described by a triple Lorentian fit function (black line). The fit parameters are reported in table 5.7, together with the relaxation times of fig. 5.18 (b):

f_- [GHz]	f_+ [GHz]	FWHM$_-$ [MHz]	FWHM$_-$ [MHz]	τ_{gr}	τ_{dec}
4.6677 ± 0.0003	4.731 ± 0.003	8.8 ± 0.8	18 ± 8	13 ± 1	19 ± 1

f_{sec} [GHz]	FWHM$_{sec}$ [MHz]
4.681 ± 0.002	50 ± 3

Table 5.7: Fit parameters (fig. 5.17).

where f_{sec} and FWHM$_{sec}$ refer to the second order magnetostatic mode. The growth and decay time are in this case not compatible because of experimental systematic errors, as not perfect compensation of the laser macro-pulse envelope, or $\delta f \neq 0$.

5.4 Discussions

In this section we demonstrate the advantage of using our method to optically drive the magnetization precession in a cavity-QED framework. Moreover, we discuss the legitimacy of attributing the photin-duced phenomenon to the opto-magnetic inverse Faraday effect, through the study of dependence to

laser beam intensity and orientation of the polarization.

5.4.1 Formalism in cavity-QED

First of all, by simmetry considerations the expression for the photoinduced non-linear magnetization derived in sec. 2.3 can be reduced to a semplified form. Provided that in our set up the laser propagation axis **k** is orthogonal to the $[110]$ crystal direction **d**, and that the reference system axes x and y coincide with **k** and **d** directions, we find that the photoinduced magnetization lies in the yz plane and reads

$$M_z = \int d\omega \Theta(\omega) |E(\omega)|^2 \cos 2\theta \tag{5.2}$$

$$M_y = \int d\omega \Theta(\omega) |E(\omega)|^2 \sin 2\theta \,, \tag{5.3}$$

where in our case $\omega = f_R$, $\Theta(\omega) \equiv \chi_{233} = -\chi_{222} = \chi_{332} = \chi_{323}$ are the non-vanishing terms of χ, $E(\omega)$ is the Fourier transform of the laser electric field and θ is the polarization angle of the incident light with respect to the y axis.
A further simplification is accomplished if we consider that in the cavity-QED configuration we drive the magnetization precession by tuning the laser repetition frequency to one of the hybridized mode frequencies, i.e. f_-. In this scondition, the real and imaginary part of the complex susceptibility $\Theta(\omega)$ can be approximated by absorption $\Theta(\omega)''$ and dispertion $\Theta(\omega)'$ [63]. In particular, at working frequency f_- we have only absorption and no dispersion, hence the the susceptivity $\Theta(\omega) = \Theta_0 f_- \pi \bar{\tau}$ becomes real, with $\bar{\tau}$ being the relaxation time of the hybridized modes. Being Θ a real variable, it therefore does not affect the magnetization direction.

5.4.2 Absorbed power

The fulfillment of resonant condition and the accomplishment of the steady-state regime with our tecnique, together with the peculiar dynamics of the hybridized system, allows us to measure a fundamental physical parameters, i.e. the total power P_a absorbed by the YIG sample during excitation. In fact, the measured power in the microwave cavity at resonance, and for a critically coupled inductive loop, is exactly $P_a/2$ A. From the measurement of P_a, we can then estimate the real parameter Θ_0 from the following expressions that is valid in our experimental conditions

$$P_a = V_s \Theta_0 (2\pi)^2 f_-^2 \bar{\tau} \frac{B_{eff}}{\mu_0} \,, \tag{5.4}$$

where B_{eff} represents the laser induced effective magnetic field and V_s the sample volume. One can show that due to $1/f$ dependence of the power spectrum generated by downconversion of the picosecond frequency comb, the infrared optical field average amplitude $B_I = \sqrt{\mu_0 I/c} = 10\,\mathrm{mT}$ at $f_o = 190 THz$ optical frequency, is suppressed to $B_{eff} = 2.5 \times 10^{-5} B_I = 0.25\,\mu\mathrm{T}$ at $f_- \approx 4.7\,\mathrm{GHz}$.
Therfore, with a measured absorbed power $P_a = (26.1 \pm 0.1)\,\mathrm{nW}$, we obtain $\Theta_0 \approx 10^8\,\mathrm{cm}^2/\mathrm{MW}$.

5.4.3 Polarization and intensity dependence

The fundamental properties of the second order non-linear IF Effect (IFE) are described by the expressions 5.2 of the photoinduced magnetization components

$$M_z = \int d\omega \Theta_0 |E(\omega)|^2 \cos 2\theta \,, \tag{5.5}$$

$$M_y = \int d\omega \Theta_0 |E(\omega)|^2 \sin 2\theta \,, \tag{5.6}$$

where we have assumed the resonant condition $f_R = f_-$. The opto-magnetic phenomenon is indeed linear-dependent to the electric field intensity, and responds to the field linear polarization with a 2θ dependence. We can perform a further simplification of the geometric description of the photoinduced magnetization vector if we realize that the cavity selects the $M_z \propto \cos 2\theta$ component via its geometric projection on the TE_{102} mode (parallel to the z direction as shown in fig. 5.1 (b)), and that the critically coupled antenna do not distinguish between parallel and antiparallel orientation of M_z. Therefore we conclude that the detected magnetization signal must be proportional to $|\cos 2\theta|$.
We then investigate the dependence of the microwave signal amplitude on the laser beam intensity and polarization, in order to confirm the initial hypothesis of non-thermal origin of the photo-induced magnetization precession and definitely attribute the observed opto–magnetic phenomenon to the inverse Faraday effect (IFE) [12].
For the polarization analysis we use Thorlabs polarizator, $\lambda/2$ plates for 1550 nm-wavelength, and analyzer.

Figures 5.19 (a), (b) show respectively the microwave signal measured in the cavity for different linear polarization angles θ, with the spherical YIG sample, and the dependence to the laser micropulse intensity I. Figure 5.20 shows the microwave signal θ-dependence with the cylindrical YIG sample.

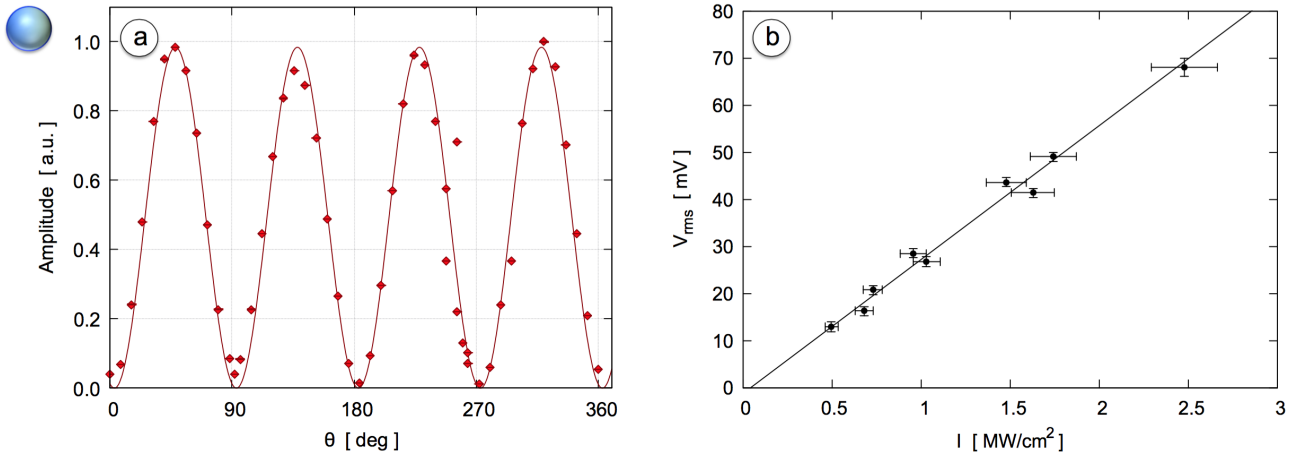

Figure 5.19: (**a**) Amplitude of the microwave power signal in the cavity as a function of the laser polarization angle, for the spherical YIG sample. (**b**) Microwave voltage signal dependence on the laser beam intensity.

In fig. 5.19 (a) the y-values of the data are measured the DFT maximum amplitude of the microwave radiated signal, and dimensionally corresponds to a microwave power. In fig. 5.20 the y-values of the data were instead measured in the time domain as voltage quantities, and then converted to powers to compare them to the previous measurements. The different tecnique justifies the larger errors. Since we deal with power, according to eq. 5.5 the dependence to θ goes like the square of a sinusoidal function. We therefore fit the data to $\propto |\cos(a\theta)|^2$, with $a_{sph,cyl}$ fit parameters for the sphere and for the cylinder respectively.
The 4–fold periodicity of the angular plots is perfectly fitted to the theoretical dependence of the photoinduced magnetization previously discussed, and the fit parameters are in good agreement with the expected value (2), as reported in table 5.8.

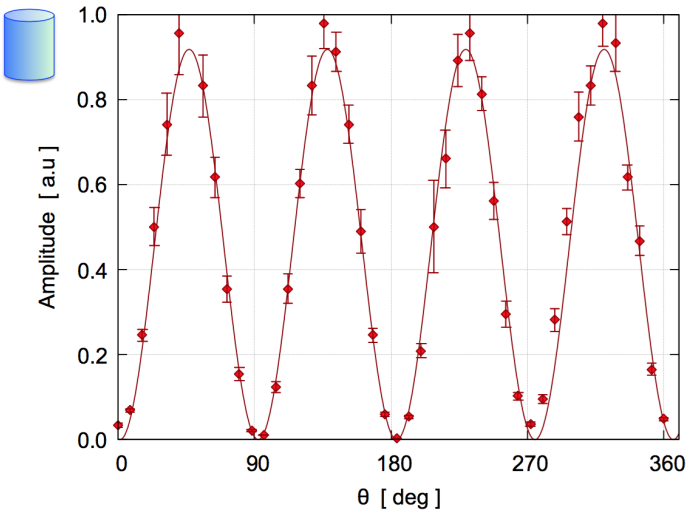

Figure 5.20: Amplitude of the microwave power signal in the cavity as a function of the laser polarization angle, for the cylindrical YIG sample.

a_{sph}	a_{cyl}	α_{lin} [mV cm^2/MW]	V_0 [mV]
2.001 ± 0.04	1.97 ± 0.04	28 ± 2	-1 ± 1

Table 5.8: Fit parameters a_{sph} (fig. 5.19 (a)), a_{cyl} (fig. 5.20) of the sinusoidal fits; angular coefficient α_{lin} and linear offset V_0 of the dependence in fig. 5.20 (b).

Finally, figure 5.19 (b) shows the linearity of the microwave signal amplitude to the laser pump intensity. The signal amplitude is measured in the steady-state regime, and the laser pump intensity is calculated from the value of the macro-pulse energy measured at the bolometer, as function of laser beam area macro-pulse time duration. The large x-errors are mainly due to the propagation on the measurement errors of beam waist and intensity. The linear dependence is in agreement with eq. 5.5 as well, and the linear coefficient α_{lin} is reported in table 5.8.

CHAPTER 6

Conclusions and Perspectives

In this thesis a full-optical, flexible tecnique to manipulate the magnetization vector in YIG based on a multi-GHz laser system has been demonstrated.
Unlike the various methods reported in the literature, we generate via the inverse Faraday effect a photoinduced microwave driving field which allows a coherent control of the magnetization in the steady-state regime. The phenomenon has been investigated both in the simplest scheme of a loop antenna coupled to the YIG samples, and in the microwave cavity scheme, which allowed an indirect measurement of the radiated field during the optically driven precession. Radiated powers in the order of several nW have been measured. Moreover, we have described how when the sample is enclosed in a cavity, the total number of involved spins can be estimated thanks to the remarkable properties of hybridization $\approx 10^{19}$. The ferromagnetic resonance parameters that we derived through optical excitation are compatible with those measured in the S-formalism. This has confirmed that we accomplished optical control of the uniform magnetization mode (FMR mode) coupled to the cavity mode. Our measurements of dependence from laser beam intensity and polarization, confirm the expected behaviour in the developed model for the IFE-based photoinduced magnetization.

As future perspectives, we intend to further develop the investigation of the phenomenon with 1064 nm-wavelength optical excitation, which belongs to the edge absorption of YIG. At this wavelength, we have indeed obtained non-trivial dependence from the polarization rotation that can not be explained by the simplified model used to explain the data at 1550 nm-wavelength. A possibility for an advanced investigation consists in equipping the apparatus for pump-and-probe analysis, in order to directly measure the induced rotation angle of the incident field polarization.
We also intend to extend the analysis to different materials, as substituted rare-earth iron garnet. YIG has in fact the great technical advantage to allow insertion of a very wide variety of cations in its garnet structure, with the possibility to achieve an enormous range of control of its magnetic properties [32]. In particular, substitution of part of the Y^{3+} on dodecahedral sites by the diamagnetic Bi^{3+} has been found to increase the Curie temperature, and has the effect of strongly enhancing the magneto-optical properties of YIG.
As final remark, it is worth mentioning that commercially available compact ultrafast oscillators with 200 pJ-energy output pulses [64] would allow to overcome the technical limits of our laser oscillator stability and further increase the flexibility of the approach, and may therefore foster applications of the presented method in the opto–magnetism field.

Appendices

APPENDIX A

Equivalent Circuit Resonator for the Driven Cavity

The equivalent circuit that models a cavity with one antenna, driven by an RF generator, is shown in fig. A.1(b) [54]. Since one antenna of the cavity in our work is undercoupled (very weakly coupled), its influence can be neglected, and the considered model suits our two-port network. Between the RF generator and the cavity there is an isolator, which is a circulator connected to a load (fig. A.1(a)). It ensures that the signals coming from the cavity are terminated in a matched load and protects the generator from reflections coming from the cavity coupler system. A lossless transmission line with a characteristic admittance G_0 connects the generator to the coupler. The cavity antenna is modeled with a transformer, allowing to match the transmission line to the cavity with an arbitrary impedence. Being V_c the voltage at the cavity terminals and G_c the cavity admittance, the total energy stored in the circuit resonator is

$$U = CV_c^2 \tag{A.1}$$

and its dissipated power is

$$P_c = G_c V_c^2/2\,. \tag{A.2}$$

Being the cavity quality factor $Q_0 = \omega_c U/P_c$, one obtains

$$Q_0 = \sqrt{\frac{C}{L}}/2\pi G_c\,. \tag{A.3}$$

Considering the cavity behaviour operating at its fundamental frequency $\omega_c = 2\pi f_c$ after the RF drive is switched off, the total power being lost will be the sum of the power dissipated in the cavity walls and the power that leaks out each antenna:

$$P_{tot} = P_c + P_e + P_T\,, \tag{A.4}$$

where P_e is associated to the input coupler and P_t to the transmitted power coupler. Analogous to the intrinsic quality factor $Q_0 = \omega_c U/P_c$, one can define the loaded quality factor

$$Q_L = \frac{\omega_c U}{P_{tot}} \tag{A.5}$$

which characterizes a cavity with couplers. Similarly one defines external quality factors Q_e and Q_t associated to each coupler. From eq. A.5 one derives the total dissipated power

$$\frac{dU}{dt} = -P_{tot} = -\frac{\omega_c U}{Q_L}\,, \tag{A.6}$$

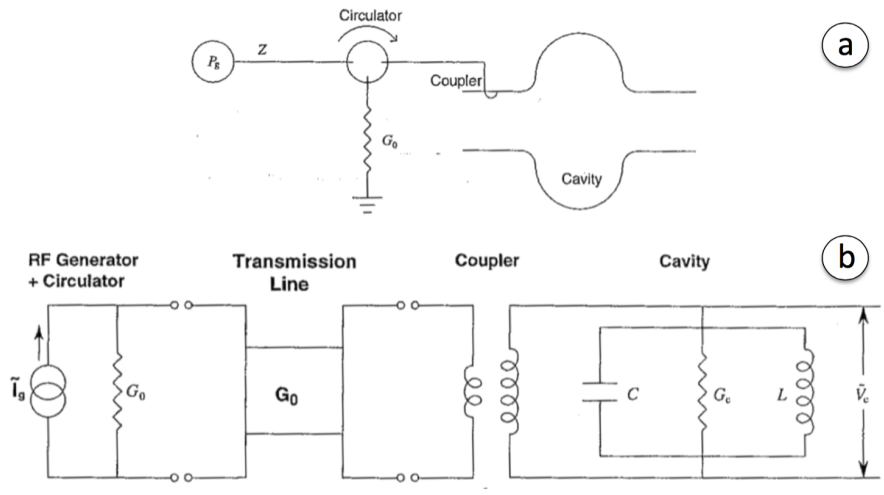

Figure A.1: (**a**) Schematic of cavity with generator and circulator. (**b**) Equivalent circuit for a cavity with one coupler being driven by an RF generator.

and if the losses are quadratic (no field emission or other anomalous losses), the soulution yields

$$U = U_0 \mathrm{e}^{\frac{-\omega_c t}{Q_L}}, \tag{A.7}$$

where U_0 is the stored energy at $t = 0$. The energy in the cavity thus decays exponentially with a time constant $\tau_L = Q_L/\omega_c$. One can define the coupling parameters, or coupling strengths of the couplers to the cavity mode as

$$\beta_e = \frac{Q_0}{Q_e} = \frac{P_e}{P_c} \tag{A.8}$$

$$\beta_e = \frac{Q_0}{Q_t} = \frac{P_t}{P_c}. \tag{A.9}$$

Therefore the β's tell how strongly the coupler interacts with the cavity. In our apparatus the fixed transmitted power probe coupling is made very weak ($\beta_t << 1$) and therefore the system can be modeled as a driven cavity with one only coupler and $\beta_e \equiv \beta$ (fig. A.1).
It is interesting to look at the case when the power P_f travelling forward through the transmission line to the cavity is a constant and the cavity is in steady state, i.e. $dU/dt = 0$. Then $U = U_0$, which can be expressed as

$$U_0 = \frac{4\beta P_f Q_0}{(1+\beta)^2 \omega_c}, \tag{A.10}$$

which is maximized when $\beta = 1$ and the cavity acts like a perfectly matched load. The reflected power is then

$$P_r = (\frac{\beta - 1}{\beta + 1})^2 P_f. \tag{A.11}$$

One derives the expression for the coupling strength

$$\beta = \frac{1 \pm \sqrt{P_r/P_f}}{1 \mp \sqrt{P_r/P_f}}. \tag{A.12}$$

Since β is always nonnegative, the upper sign is used when $\beta > 1$ (overcoupled), and the lower sign for $\beta < 1$ (undercoupled).

When the RF drive P_f is turned off at $t = 0$, the instantaneous equilibrium value of the stored energy becomes $U_0 = 0$, and one can derive β through the ratio of the drive RF and the instantaneous emitted power by

$$\beta = \frac{1}{2\sqrt{\frac{P_f}{P_e}} - 1}. \tag{A.13}$$

Oppositely, when the RF drive P_f is turned on at $t = 0$, U rises untill it reaches the equilibrium value U_0.

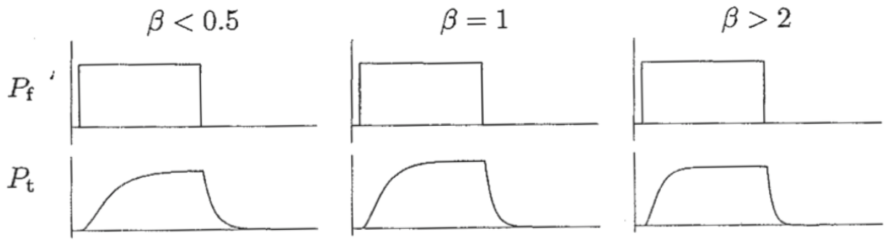

Figure A.2: Rectangular drive pulses and their effects on the cavity for three different values of coupling.

Considering those two cases, figure A.2 shows the power measurements in the time domain (with an oscilloscope) for three different input coupling strengths, when the cavity is driven by a rectangular pulse P_f of a long enough length to drive the cavity to near equilibrium. The stored energy is measured by measuring the transmitted power P_t via the weakly coupled probe.

In general, for measurements in the frequency domain, the coupling strengths of the couplers together with the cavity loss cause the resonance to be broadened in frequency. The FWHM of the resonance is $1/\tau_L$, i.e. $Q_L = \omega/2\Delta\omega$, where $\Delta\omega$ is half the resonance width.

Bibliography

[1] C. D. Stanciu, F. Hansteen, A. V. Kimel, A. Kirilyuk, A. Tsukamoto, A. Itoh, and T. Rasing, *Phys. Rev. Lett.* **99**, 047601 (2007).

[2] T. Li, A. Patz, L. Mouchliadis, J. Yan, T. A. Lograsso, I. E. Perakis, and J. Wang, *Nature* **496**, 69 (2013).

[3] Z.-L. Xiang, J. Q. You, and F. Nori, Hybrid quantum circuits: superconducting circuits interacting with other quantum systems, *Rev. of Mod. Phys.* **85**, 623 (2013).

[4] D. Zhang, X.-M. Wang, T.-F. Li, X.-Q. Luo, W. Wu, F. Nori, and JQ You, Cavity quantum electrodynamics with ferromagnetic magnons in a small yittrium-iron-garnet sphere, *npj Quantum Information* **1**, (2015).

[5] R. P. Feynman, R. B. Leighton, and M. Sands, The Feynman lectures on physics, the definitive edition vol. 2 (*Pearson Education Inc.*, 2006).

[6] F. Bloch, Nuclear induction, *Phys. Rev.* **70**, 460 (1946).

[7] N. Bloembergen, and R. V. Pound, Radiation damping in magnetic resonance experiments, *Phys. Rev.* **95**, 8 (1954).

[8] W. E. Bell, and A. L. Bloom, Optically driven spin precession, *Phys. Rev. Lett.* **6**, 280 (1961).

[9] S. Bloom, Effects of radiation damping on spin dynamics, *J. Appl. Phys.* **28**, 800 (1957).

[10] G. Suryan, Nuclear magnetic resonance and the effect of the methods of observation, *Current Sci.* **18**, 203 (1949).

[11] C. Kittel, Introduction to solid state phyisics, 8th edition (*Jhon Wiley & Sons Inc.*, 2005).

[12] A. Kirilyuk, A. V. Kimel, and T. Rasing, Ultrafast optical manipulation of magnetic order, *Reviews of Mod. Phys.* **82**, 2731 (2010).

[13] E. Beaurepaire, J.-C. Merle, A. Daunois, and J.Y. Bigot, Ultrafast spin dynamics in ferromagnetic nickel, *Phys. Rev. Lett*. **76**, 4250 (1996).

[14] L. Guidoni, E. Beaurepaire, and J.-Y. Bigot, Magneto-optics in the ultrafast regime: thermalization of spin populations in ferromagnetic films, *Phys. Rev. Lett.* **89**, 017401 (2002).

[15] E. Beaurepaire, G. M. Turner, S. M. Harrel, M. C. Beard, J. Y. Bigot, and C. A. Schmuttenmaer, Coherent terahertz emission from ferromagnetic films excited by femtosecond laser pulses, *Appl. Phys. Lett.* **84**, 3465 (2004).

[16] J.-Y. Bigot, L. Guidoni, E. Beaurepaire, and P. N. Saeta, Femtosecond spectrotemporal magneto-optics, *Phys. Rev. Lett.* **93**, 077401 (2004).

[17] A. F. Kabychenkov, Magnetic phase transitions in a light wave, *Sov. Phys. JETP* **73**, (1991).

[18] P. S. Pershan, Nonlinear optical properties of solids: energy considerations, *Phys. Rev.* **130**, 919 (1963).

[19] L. D. Landau, E. M. Lifshitz, and L. P. Pitaevskii, Electrodynamics of continuous media, 2nd edition (*Butterworth & Heinemann*, 1984).

[20] L. P. Pitaevskii, The problem of the form of the spectrum of elementary excitations of liquid helium II, *JETP* **12**, 1008 (1961).

[21] J. P. van der Ziel, P. S. Pershan, and L. D. Malmstrom, Optically-induced magnetization resulting from the inverse Faraday effect, *Phys. Rev. Lett.* **15**, 190 (1965).

[22] A. V. Kimel, A. Kirilyuk, P. A. Usachev, R. V. Pisarev, A. M. Balbashov and T. Rasing, Ultrafast non-thermal control of magnetization by instantaneous photomagnetic pulses, *Nature* **435**, 655 (2005).

[23] S. Ali, J. R. Davies, and J. T. Mendonca, Inverse Faraday effect with linearli polarized laser pulses, *Phys. Rev. Lett.* **105**, 035001 (2010).

[24] N. Kanda, T. Higuchi, H. Shimizu, K. Konishi, K. Yoshioka, and M. Kuwata-Gonokami, The vectorial control of magnetization by light, *Nature Commun.* **2**, 362 (2011).

[25] U. Keller, *Nature* **424**, 831 (2003).

[26] S. T. Cundiff, and J. Ye, Femptosecond optical frequency combs, *Rev. of Mod. Phys.* **75**, 325 (2003).

[27] G. L. Matthaei, L. Young, and E. M. T. Jones, Design of microwave filters, impedance-matching networks, and coupling structures, (*Stanford Research Institute*, 1963).

[28] F. R. Morgenthaler, Steerable volume and surface spin waves in ferrimagnetic films, *Technical Report* **2**, (1970).

[29] B. Lax, and K. J. Button, Microwave ferrites and ferrimagnetics, (*McGraw-Hill Book Co. Inc.*, 1961).

[30] J. A. Osborn, Demagnetizing factors of the general ellipsoid, *Phys. Rev.* **67**, 351(1945).

[31] J. F. Dillon, Ferrimagnetic resonance in Yittrium Iron Garnet, *Phys. Rev.* **105**, 759 (1957).

[32] F. Hansteen, Ultrafast Optical Manipulation in Ferrimagnetic Garnets, PHD thesis, (Radboud Universiteit Nijmegen, 4 July 1975, Norway).

[33] G. Winkler, Magnetic Garnets, (Friedr. Vieweg & Sohn, Braunschweig, Germany, 1981).

[34] A. Paoletti, Physics of Magnetic Garnets, Enrico Fermi International School of Physics, Italian Physical Society, (North-Holland Publishing Co., 1978).

[35] M. A. Gilleo, and S. Geller, Magnetic and crystallographic properties of substituted Yttrium-Iron Garnet *Phys. Rev.* **110**, 73 (1958).

[36] G. A. Novak, and G. V. Gibbs, The crystal chemistry of the silicate garnets, *Amer. Mineralog.* **56**, 791 (1971).

[37] P. C. fletcher, and R. O. Bell, Ferrimagnetic resonance modes in spheres, *Jour. Appl. Phys.* **30**, 687 (1959).

[38] P. C. fletcher, and I. H. Solt, Coupling of the magnetostatic modes, *Jour. Appl. Phys.* **30**, 181S (1959).

[39] A. E. H. Love, A Treatise on the Mathematical Theory of Elasticity, 4th edn. (*Cambridge, UK: University Press.*, 2013).

[40] W. Voigt, Lehrbuch der Kristallphysik, reprint of 1st edition (*Teubner: Leipzig*, 1928).

[41] S. R.-K. Rodriguez, Classical and quantum distinctions between weak and strong coupling, *Eur. J. Phys.* **37**, 025802 (2016).

[42] D. Dragoman, and M. Dragoman, Quantum-Classical Analogies, The Frontiers Collection (*Berlin: Springer*, 2014).

[43] L. Novotny, Strong coupling, energy splitting, and level crossings: a classical perspective, *Am. J. Phys.* **78**, 1199 (2010).

[44] L. C. Andreani, Exciton-polaritons in bulk semiconductors and in confined electron and photon systems Strong Light-Matter Coupling, (*Singapore: World Scientific*, 2013).

[45] F. P. Laussy, E. del Valle, and C. Tejedor, Luminescence spectra of quantum dots in microcavities: I. Bosons, *Phys. Rev. B* **79**, 235325 (2009).

[46] M. W. Doherty, N. B. Manson, P. Delaney, F. Jelezko, J. Wrachtrup, and L. C.L. Hollenberg, The nitrogen-vacancy colour centre in diamond, *Physics Reports* **528**, 1 (2013).

[47] H. Huebl, C. W. Zollitsch, J. Lotze, F. Hocke, M. Greifenstein, A. Marx, R. Gross, and S. T.B. Goennenwein, High cooperativity microwave resonator ferrimagnetic insulator hybrids, *Phys. Rev. Lett.* **111**, 127003 (2013).

[48] X. Zhang, C.-L. Zou, L. Jiang, and H. X. Tang, Strongly coupled magnons and cavity microwave photons, *Phys. Rev. Lett.* **113**, 156401 (2014).

[49] Y. Tabuchi, S. Ishino, T. Ishikawa, R. Yamazaki, K. Usami, and Y. Nakamura, Hybridizing ferromagnetic magnons and microwave photons in the quantum limit, *Phys. Rev. Lett.* **113**, 083603 (2014).

[50] G. S. Agarwal, Vacuum-field Rabi splittings in microwave absorption by Rydberg atoms in a cavity, *Phys. Rev. Lett.* **53**, 1732 (1984).

[51] A. Imamoglu, cavity QED based on collective magnetic dipole coupling: spin ensembles as hybrid two.level systems, *Phys. Rev. Lett.* **102**, 083602 (2009).

[52] Ö. O. Soykal, and M. E. Flatté, Strong field interactions between a nanomagnet and a photonic cavity, *Phys. Rev. Lett.* **104**, 077202 (2010).

[53] D. F. Walls, and G. J. Milburn, Quantum optics, 1st edition (*Springer*, 1994).

[54] H. Padamsee, J. Knobloch, and T. Hays, RF superconductivity for accelerators, (*John Wiley & Sons Inc.*, 1998).

[55] A. A. Clerk, S. M. Girvin, F. Marquardt, and R. J. Schoelkopf, Introduction to quantum noise, measurement, and amplification, *Rev. Mod. Phys.* **82**, 1155 (2010).

[56] F. Caspers, Ferromagnetic resonance (FMR) - A method to measure magnetic fields in accelerator environment (first result from PS), 55*th PS/AR scientific meeting*, (1994).

[57] A. Agnesi, F. Pirzio, A. Tomaselli, G. Reali, and C. Braggio, Multi-GHz tunable-repetition-rate mode-locked Nd:$GdVO_4$ laser, *Optics Express* **13**, 5302-5307 (2005).

[58] A. Agnesi, C. Braggio, et al., Laser system generating 250-mJ bunches of 5-GHz repetition rate, 12-ps pulses, *Opt. Expr.* **16**, 15811 (2008).

[59] A. Agnesi, L. Carrà, F. Pirzio, D. Scarpa, A. Tomaselli, G. Reali, C. Vacchi, and C. Braggio, High-gain diode-pumped amplifier for generation of microjoule-level picosecond pulses, *Optics Express* **14**, 9244-9249 (2006).

[60] A. Agnesi, C. Braggio, et al., A laser system for the parametric amplification of electromagnetic fields in a microwave cavity, *Rev. Scient. Instr.* **82**, 115107 (2011).

[61] Braggio, et al., Optical manipulation of a magnon-photon hybrid system, arXiv:1609.08147v1, (2016).

[62] L. M. Frantz, and J. S. Nodvik, Theory of pulse propagation in a laser amplifier, *J. Appl. Phys.* **34**, 2346-2349 (1963).

[63] F. Fiorillo, Characterization and measurement of magnetic materials (*Elsevier*, 2004).

[64] L. Krainer, R. Paschotta, S. Lecomte, M. Moser, K. J. Weingarten, and U. Keller, Compact Nd:YVO_4 lasers with pulse repetition rates up to 160 GHz, *IEEE J. Quantum Electron.* **38**, 1331-1338 (2002).